Monthly Notices of the ROYAL ASTRONOMICAL SOCIETY

MNRAS **503,** 5006–5024 (2021) doi:10.1093/mnras/stab596
Advance Access publication 2021 March 16

Characterizing the magnetic fields of nearby molecular clouds using submillimeter polarization observations

Colin H. Sullivan,[1,2]★ L. M. Fissel,[2,3]★ P. K. King,[1,4,5] C.-Y. Chen,[1]★ Z.-Y. Li[1] and J. D. Soler[6]

[1]*Department of Astronomy, University of Virginia, Charlottesville, VA 22904, USA*
[2]*National Radio Astronomy Observatory, Charlottesville, VA 22904, USA*
[3]*Department of Physics, Engineering Physics, and Astronomy, Queen's University, Kingston, ON K7L 3N6, Canada*
[4]*Johns Hopkins University Applied Physics Laboratory, Laurel, MD, 20723*
[5]*Lawrence Livermore National Laboratory, Livermore, CA 94550, USA*
[6]*Max Planck Institute for Astronomy, Königstuhl 17, D-69117 Heidelberg, Germany*

Accepted 2021 February 23. Received 2021 February 21; in original form 2019 October 30

ABSTRACT

Of all the factors that influence star formation, magnetic fields are perhaps the least well understood. The goal of this paper is to characterize the 3D magnetic field properties of nearby molecular clouds through various methods of statistically analysing maps of polarized dust emission. Our study focuses on nine clouds, with data taken from the *Planck* Sky Survey as well as data from the Balloon-borne Large Aperture Submillimeter Telescope for Polarimetry observations of Vela C. We compare the distributions of polarization fraction (p), dispersion in polarization angles ($\mathcal{S}$), and hydrogen column density ($N_{\rm H}$) for each of our targeted clouds. To broaden the scope of our analysis, we compare the distributions of our clouds' polarization observables with measurements from synthetic polarization maps generated from numerical simulations. We also use the distribution of polarization fraction measurements to estimate the inclination angle of each cloud's cloud-scale magnetic field. We obtain a range of inclination angles associated with our clouds, varying from 16° to 69°. We establish inverse correlations between p and both $\mathcal{S}$ and $N_{\rm H}$ in almost every cloud, but we are unable to establish a statistically robust $\mathcal{S}$ versus $N_{\rm H}$ trend. By comparing the results of these different statistical analysis techniques, we are able to propose a more comprehensive view of each cloud's 3D magnetic field properties. These detailed cloud analyses will be useful in the continued studies of cloud-scale magnetic fields and the ways in which they affect star formation within these molecular clouds.

Key words: magnetic fields – polarization – ISM: Clouds.

1 INTRODUCTION

Molecular clouds (MCs) are the birthplaces of stars. These clouds are typically cold (10–30K) and have dense sub-regions within them that may collapse under gravity to form stars. The evolution and efficiency of star formation within MCs are regulated by a number of factors, primarily gravity, turbulence, and magnetic fields (McKee & Ostriker 2007). Among these physical processes, magnetic fields are perhaps the least well understood, and this is largely because magnetic fields are very difficult to observe directly. Although the line-of-sight component of a magnetic field can be measured by Zeeman spectral line splitting (Crutcher 2012), the width of the line splitting is typically much less than the thermally broadened line width, which makes detection of Zeeman splitting extremely difficult. The long observation times required also make Zeeman observations impractical for producing cloud-scale maps.

As an alternative, linearly polarized thermal dust emission is commonly used to create large-scale maps to study MC-scale magnetic fields. This technique relies heavily on the orientation of their dust grains, as dust grains tend to align with their minor axes oriented parallel to the local magnetic field lines. This alignment is most likely caused by radiative torques from the local radiation field (see Andersson, Lazarian & Vaillancourt 2015, for a review). This process creates a net linear polarization orientation of the emitted light that is perpendicular to the magnetic field direction projected on the sky.

By measuring linear polarization of the sub-mm radiation emitted by dust grains within the MC and rotating the polarization orientation by 90°, we can map the corresponding magnetic field orientation projected on the plane of sky. These measured orientation values represent the averaged magnetic field orientation within the volume of the cloud probed by the telescope beam, and are most sensitive to regions of high dust emissivity and efficient grain alignment.

In addition to the inferred plane-of-sky magnetic field orientation, there are several other polarization parameters that can be used to study the structure and geometry of magnetic fields in MCs. The polarization fraction (p) of the emission is the fraction of observed radiation that is linearly polarized. p is sensitive to the efficiency with which grains are aligned with respect to the magnetic field, the degree of disorder in the plane-of-sky magnetic field within the dust column probed by the polarimeter, and the inclination angle of the cloud's magnetic field with respect to the plane of the sky. In addition, the local polarization angle dispersion ($\mathcal{S}$) is used to measure the disorder in the projected magnetic field orientation at

★ E-mail: colin.sullivan@virginia.edu (CHS); laura.fissel@queensu.ca (LMF); cc6pg@virginia.edu (C-YC)

a given location in the cloud (Fissel et al. 2016). In addition to these polarimetric properties, we also consider the hydrogen column density ($N_{\rm H}$) in our analysis. This quantity is used as a proxy for the total mass surface density of our clouds, and is thus useful for characterizing the gas substructure of MCs.

Lower resolution polarization studies, such as the 1° resolution, all-sky analysis of Planck Collaboration XIX (2015a), or the Balloon-borne Large Aperture Submillimeter Telescope for Polarimetry (BLASTPol) 2.′5 resolution study of the Vela C giant molecular cloud (GMC; Fissel et al. 2016), have identified several correlations between p, $\mathcal{S}$, and $N_{\rm H}$. The first trend is a negative correlation between p and $\mathcal{S}$: as $\mathcal{S}$ increases, p decreases. This trend could be related to the differences in the 3D geometry of the magnetic field in different parts of the cloud as p is proportional to $\cos^2\gamma$, where γ is the inclination angle of the magnetic field with respect to the plane of the sky (Hildebrand 1988). For cloud sightlines where the magnetic field is nearly parallel to the line of sight, p values tend to be lower, and upon projection on to the plane-of-sky the angles can vary greatly between adjacent sightlines, leading to large values of $\mathcal{S}$.

In addition, a weak, disordered magnetic field provides little resistance to turbulent motions, and can be easily driven to a highly disordered state, which produces large values for $\mathcal{S}$. This in turn leads to significantly lower p values. Strong magnetic fields are able to resist turbulent motions that are perpendicular to their field lines, and thus tend to have lower values for $\mathcal{S}$. Low-p and high-$\mathcal{S}$ values can therefore indicate a weak/disordered magnetic field and/or a nearly line-of-sight magnetic field orientation, while high p values and low $\mathcal{S}$ values can indicate a strongly ordered magnetic field and/or a nearly plane-of-sky magnetic field orientation.

The second observed trend that we will investigate is the anticorrelation between polarization fraction p and hydrogen column density $N_{\rm H}$ (Planck Collaboration XIX 2015a; Fissel et al. 2016). Dust grains are believed to be aligned with respect to the local magnetic fields by the effect of radiative torques (Andersson et al. 2015). This process may become less efficient in regions of high column density because photons that can provide these alignment torques are more likely to be scattered and/or absorbed within higher column density sightlines (King et al. 2019). This shielding process thus results in lower p values in regions of high $N_{\rm H}$ (Planck Collaboration XIX 2015a; Planck Collaboration XX 2015b). In King et al. (2018), this correlation could not be explained purely in terms of magnetic field alignment or strength alone, but it was found in King et al. (2019) that introducing grain alignment efficiency may be able to explain it. Correlations between $\mathcal{S}$ and $N_{\rm H}$ have not to date been firmly established (Fissel et al. 2016), and so we attempt to contribute to this debate through 2D Kernel Density Estimates involving these two variables.

In King et al. (2018), the authors examined synthetic polarization observations of two magnetized cloud formation simulations generated using the `Athena` magnetohydrodynamic (MHD) code (Chen, King & Li 2016), with the goal of reproducing the correlations between p, $N_{\rm H}$, and $\mathcal{S}$ found in observations of the Vela C GMC in Fissel et al. (2016). In order to reproduce the high levels of $\mathcal{S}$, large range of p, and the level of anticorrelation between p and $\mathcal{S}$, the authors speculated that Vela C must have either a weak magnetic field or a stronger field that is highly inclined with respect to the plane of the sky. Other studies analysing the orientation of cloud structure with respect to the magnetic field (Soler et al. 2017; Fissel et al. 2019) have suggested that Vela C has a reasonably strong cloud-scale magnetic field, and so it seems more likely that Vela C's magnetic field must be significantly inclined with respect to the plane of the sky (King et al. 2018; Chen et al. 2019).

Here, we extended the comparisons of the p, $N_{\rm H}$, and $\mathcal{S}$ distributions to a larger sample size of MCs by including *Planck* 353 GHz polarization observations of eight nearby clouds. In this way, we will determine if the results of King et al. (2018) are consistent with a larger sample size of nearby MCs. The eight *Planck* clouds included in this study are all nearby and relatively low mass, while Vela C is more distant and massive ($M_{\rm Vela} > 10^5\,{\rm M}_\odot$). Significantly higher resolution (2.5 arcmin as opposed to 15 arcmin for the *Planck* observations) means that Vela C has a linear resolution almost equal to the closest of the *Planck* clouds. Linear resolution and other such cloud-specific quantities are listed in Table 1.

In this paper, we use our increased sample size to provide more stringent tests of the analyses presented in King et al. (2018, 2019), Chen et al. (2019), and Fissel et al. (2019). We also compare our results to multiple intermediate-results *Planck* papers, specifically Planck Collaboration XX (2015b), Planck Collaboration XIX (2015a) and Planck Collaboration XII (2018). This paper is organized as follows: Section 2 – observations and data reduction, Section 3 – comparison of polarization properties between different clouds, Section 4 – comparison with synthetic polarization observations of 3D MHD simulations reported in King et al. (2018), and Section 5 – conclusions. In Appendix A, we discuss how our results are influenced by different methods selecting cloud sightlines.

2 OBSERVATIONS AND DATA REDUCTION

In this paper, we analyse thermal dust emission polarization observations of nine nearby MCs. For eight of the clouds, we use 353 GHz polarization maps from the *Planck* satellite, first presented in Planck Collaboration XXXV (2016). Our study includes the same set of MCs as Planck Collaboration XXXV (2016; Aquila Rift, Cepheus, Chamaeleon-Musca, Corona Australis, Lupus, Ophiuchus, Perseus, and Taurus), with the exception of the Orion MC and IC5146. IC5146 was excluded as it is fairly close to the Galactic plane, and as such its Stokes Q and U maps had comparable signal to the *Planck* polarization maps of diffuse interstellar medium (ISM) at the same Galactic latitudes. Orion was excluded because it is an evolved, high-mass star-forming region, where the magnetic field geometry has likely been strongly affected by feedback from previous high mass star formation (Soler, Bracco & Pon 2018). We compare these *Planck* polarization maps to 500 μm polarization maps of the Vela C cloud, obtained with the higher resolution BLASTPol (Galitzki et al. 2014; Fissel et al. 2016), which mapped four of the five sub-regions of Vela C identified by Hill et al. (2011): the South-Nest (SN), South-Ridge (SR), Centre-Nest (CN), and Centre-Ridge (CR). This young GMC has a comparable mass to Orion at $M \sim 10^5\,{\rm M}_\odot$ (Yamaguchi et al. 1999), but it is further away ($d \sim 933$ pc; Fissel et al. 2019) and appears to be much less evolved compared to the Orion MC (Hill et al. 2011).

The *Planck* data include individual maps of column density of atomic hydrogen $N_{\rm H}$ and the linear Stokes parameters I, Q, and U. The Stokes I, Q, and U were mapped to a full width at half-maximum (FWHM) resolution of 15 arcmin, while the column density maps have a higher resolution of 5 arcmin. The higher resolution $N_{\rm H}$ maps were derived from spectral fits to total intensity maps, which have a much higher SNR than the polarization data. In Table 1, we list the distance to each cloud and the corresponding linear resolution of each polarization map, which range from 0.6 pc (Taurus, Lupus, Ophiuchus) to 2.1 pc (Aquila Rift).

Using these data, we created maps of polarization fraction (p) and dispersion in polarization angles ($\mathcal{S}$). The p maps were created using

$$p = \frac{\sqrt{Q^2 + U^2}}{I}. \quad (1)$$

Table 1. This table displays the geometric mean (μ_G), median, and arithmetic standard deviation value (σ) of each cloud's logarithm of the hydrogen column density N_H, as well as the threshold values used to mask cloud regions with low N_H as described in Section 2.1. Also listed are the distance to each cloud, the corresponding linear resolution of each observation, and the total observed area for each cloud. The distance measurements are the median of the *Gaia*-informed, reddening-based distances towards different cloud sightlines from Zucker et al. (2019), each of which has $\leq 10\%$ errors. Note that some clouds such as the Aquila Rift and Cepheus contain molecular cloud structures at very different distances.

	$\mu_G(\log(N_H/\mathrm{cm}^{-2}))$	$\log(N_{H,\mathrm{med}}/\mathrm{cm}^{-2})$	$\sigma_{\log(N_H/\mathrm{cm}^{-2})}$	Threshold $(\log(N_H/\mathrm{cm}^{-2}))$	Distance (pc)	Lin. res. (pc)	Obs. area (pc^2)
AquilaRift	21.79	21.84	0.26	21.26	477	2.1	8329
Cepheus	21.43	21.47	0.19	20.88	375	1.6	15 910
Chamaeleon-Musca	21.17	21.18	0.18	20.80	190	0.8	2104
Corona Australis	20.99	20.95	0.21	20.73	155	0.7	1302
Lupus	21.39	21.39	0.20	20.98	160	0.7	883
Ophiuchus	21.40	21.39	0.24	20.75	139	0.6	1042
Perseus	21.33	21.32	0.27	20.72	284	1.2	2244
Taurus	21.49	21.48	0.24	20.79	148	0.6	1611
Vela C	22.04	22.04	0.38	21.60	931	0.7	1136

$\mathcal{S}$ was calculated by taking the difference in the polarization angles for all points within a specified lag scale around each pixel, as discussed in appendix D of Planck Collaboration XXXV (2016):

$$\mathcal{S}(x,\delta) = \sqrt{\frac{1}{N}\sum_{i=1}^{N}(\Delta\Psi_{x,i})^2}, \tag{2}$$

where δ is the lag scale and

$$\Delta\Psi_{x,i} = \frac{1}{2}\arctan(Q_iU_x - Q_xU_i,\ Q_iQ_x + U_iU_x) \tag{3}$$

is the difference in polarization angle between a given map location x and a nearby map location i. The lag scale we used in our calculations of $\mathcal{S}$ was equal to each observation's resolution: 15 arcmin for the *Planck* clouds, and 2.5 arcmin for Vela C. The population statistics of p and $\mathcal{S}$ are presented below in Table 2.

The column density map of Vela C was derived from dust spectral fits to total intensity maps at 160, 250, 350, and 500 μm from the *Herschel* telescope and smoothed to 2.5 arcmin FWHM resolution, as described in Fissel et al. (2016). Following the convention in Planck Collaboration XXXV (2016), the column density maps from *Planck* were derived from a 353 GHz optical depth (τ_{353}) map (Planck Collaboration XI 2014), using the relationship

$$\tau_{353}/N_H = 1.2\times10^{-26}\,\mathrm{cm}^2, \tag{4}$$

while τ_{353} was derived from fits to the 353, 545, and 857 GHz *Planck* and IRAS 100 μm observations using a modified blackbody spectrum. We note that Planck Collaboration (2014) finds variations in dust opacity versus N_H, especially between the diffuse and denser phases of the ISM (with the transition at approximately $N_H \approx 10^{21}\,\mathrm{cm}^{-2}$), but we note that our applied column density threshold excludes most diffuse ISM sightlines.

Note that though the BLASTPol polarization maps of Vela C have a resolution of 2.5 arcmin, which is higher than the 15 arcmin resolution of the *Planck* maps, the linear resolution is comparable to those of the nearer MCs observed with *Planck* (see Table 1) because Vela C is much further away.

2.1 Sightline selection criteria

Selecting a limited number of sightlines is important in this analysis, as we are attempting to analyse solely the polarization properties of MCs, unlike other studies which include diffuse ISM sightlines in their analysis (Planck Collaboration XII 2018). We therefore apply cuts to remove sightlines where the polarization signal is likely to be tracing mostly the more diffuse ISM, or have low signal to noise.

Our goal is to only select sightlines where the dust emission is likely to be dominated by the cloud rather than foreground or background dust. While this process is necessary to exclude the diffuse ISM surrounding our target clouds, it also serves to remove sightlines that have low degrees of statistical significance and would therefore necessitate the debiasing of the polarization data. For more details on the ways in which our masking affects our results, see Appendix A.

We find these target regions by first comparing the mean N_H of our *Planck* maps to those of diffuse dust emission. Planck Collaboration XXXV (2016) estimated the contribution of background/foreground dust by observing a relatively empty area of the sky at the same Galactic latitude as each of their clouds, and assuming that the mean N_H value in this reference region represented the mean N_H of the diffuse ISM around said cloud. We have used the same reference maps in our analysis to identify threshold column density levels for each cloud, which are listed in Table 1. We compare the N_H of each cloud to the threshold value derived from its corresponding reference region: any pixel in a cloud's column density map (smoothed to 15 arcmin FWHM) that was below this cut-off value was masked, and therefore excluded from future analysis.[1]

In addition, we applied polarization-based cuts to ensure that the sightlines we were evaluating have statistically significant polarization detections. We compared the strength of each sightline's polarized intensity (P) to its uncertainty and masked out any sightlines for which

$$\frac{P}{\sigma_P} < 3, \tag{5}$$

where σ_P is the uncertainty in P. Fig. 1 shows the p maps for the dust sightlines that pass all of our selection criteria. Because Vela C is near the Galactic plane, the values included in this study also only include the regions within the dense cloud sub-regions defined by

[1]Note that the 1D column density PDFs shown in Fig. 4 do not include any sightline cuts. This was done in order to show the distribution of the cloud column density unbiased by the cloud polarization levels. The background N_H threshold levels for each cloud are presented in Table 1 and indicated in the top row of Fig. 4 with the dashed vertical lines.

Table 2. The geometric mean, median, arithmetic, and log of geometric standard deviation, for both the p and $\mathcal{S}$ polarization parameters. The notation is chosen to match those used in King et al. (2018), Table 7: $\mu_G(p)$ represents the geometric mean of p, p_{med} represents the median of p, σ_p represents the standard deviation of p, and $\log \sigma_G(p)$ represents the log of the geometric standard deviation of p. The same notation format is applied to both $\mathcal{S}$ and N_H throughout this paper.

	$\mu_G(p)$	p_{med}	σ_p	$\log \sigma_G(p)$	$\mu_G(\mathcal{S})$	$\mathcal{S}_{med}$	$\sigma_\mathcal{S}$	$\log \sigma_G(\mathcal{S})$
AquilaRift	0.037	0.044	0.023	0.282	5.30°	4.84°	7.67°	0.326
Cepheus	0.046	0.047	0.026	0.223	5.62°	5.43°	5.86°	0.290
Chamaeleon-Musca	0.084	0.091	0.030	0.174	3.80°	3.62°	6.61°	0.276
Corona Australis	0.069	0.075	0.030	0.208	7.19°	6.90°	6.61°	0.270
Lupus	0.044	0.047	0.022	0.216	7.68°	7.48°	8.35°	0.310
Ophiuchus	0.050	0.051	0.029	0.240	7.34°	7.18°	8.34°	0.312
Perseus	0.039	0.038	0.027	0.248	11.13°	10.93°	9.43°	0.280
Taurus	0.048	0.050	0.024	0.212	6.54°	6.29°	6.27°	0.276
Vela C	0.033	0.032	1.1	0.368	10.26°	9.36°	10.31°	0.295

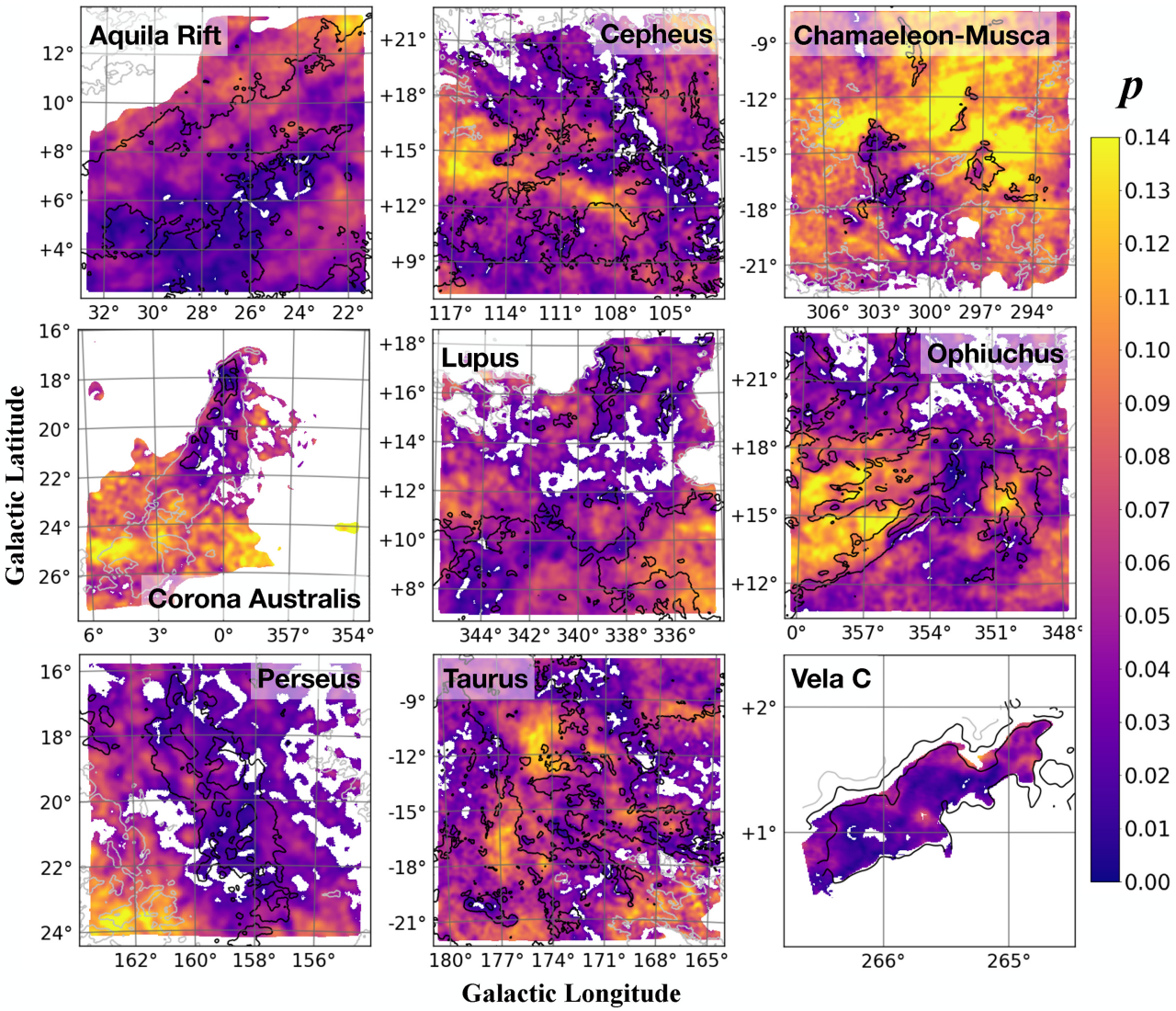

Figure 1. Maps of polarization fraction, as calculated using equation (1). Each map has been masked according to the process described in 2.1. Contours are shown for N_H. The three contour levels are $\log(N_H/\mathrm{cm}^{-2}) = 21$ (*grey*), 21.5 (*black*), and 22 (*black*). Throughout this paper, 'log' will be used to mean 'log base 10' ($\log_{10}$).

Hill et al. (2011), where the contribution from the diffuse ISM along the same sightlines is not significant.

We note that our sightline selection will tend to bias our observations towards regions of higher polarization fraction. The cuts based on column density eliminate low-column dust sightlines where the polarization fraction tends to be high. However, the cuts based on polarized intensity tend to eliminate a larger fraction of sightlines with low p and high $\mathcal{S}$ in intermediate and high column density

regions. We discuss in detail how different choices of sightline selection method affect our results in Appendix A.

3 COMPARISON OF POLARIZATION PROPERTIES

In this section, we present our analysis of the *Planck* polarimetric data. Note that though we are investigating regions that have been previously studied in Planck Collaboration XIX (2015a), Planck Collaboration XX (2015b), and Planck Collaboration XII (2018), the *Planck* papers aimed to characterize the magnetic fields in molecular gas clouds while also including sightlines that probe the diffuse ISM. In contrast, we have attempted to only select sightlines where the dust emission is associated with these particular MCs. Furthermore, our sightline masking strategy described in Section 2.1 predominantly removes sightlines with low polarization fraction (p). By masking out low polarization regions in an attempt to reduce the contributions of background noise, we correspondingly mask out the regions of highest dispersion in polarization angles ($\mathcal{S}$). This masking process thus leads to us having significantly lower $\mathcal{S}$ values than those recorded in the *Planck* papers. The effects of sightline selection choices on our results are discussed in more detail in Appendix A.

We also note that there is a difference in resolution and lag scale (δ) between our work and previous studies. Planck Collaboration XIX (2015a) and Planck Collaboration XX (2015b) state that $\mathcal{S}$ increases with δ. Thus, the resolution and δ used in Planck Collaboration XIX (2015), a resolution of 1° and $\delta = 30$ arcmin, are likely to produce higher $\mathcal{S}$ values than our study, which used resolution values of 15 arcmin (*Planck*) and 2.5 arcmin (BLASTPol) for their corresponding lag scales. This effect likely decreased our $\mathcal{S}$ values compared to Planck Collaboration XIX (2015a), but Planck Collaboration XX (2015b) uses the same resolution of 15 arcmin as ours, and a very comparable lag scale of $\delta = 16$ arcmin. This means that the difference in $\mathcal{S}$ values between our study and those of Planck Collaboration XX (2015b) will be almost entirely due to the differences in masking.

3.1 Probability distributions of polarimetric observables

We first compare the properties of each cloud by considering the distribution of our three observable values, $N_{\rm H}$, p, and $\mathcal{S}$, individually. These plots were created using a Gaussian KDE from the `astropy.convolution` package in PYTHON (Astropy Collaboration 2013; Price-Whelan et al. 2018), which takes an input variable and calculates its probability density function (PDF). These PDFs provide the relative probability density, which we refer to as $f(x)$, at all values, which is a measure of how likely a random data point is to fall within the given range of x values. Fig. 4 shows the PDFs for $N_{\rm H}$, p, and $\mathcal{S}$ on a logarithmic scale.

The PDFs are useful as they provide a basic characterization of the population of each observable's distribution, including its width and peak (most probable value) within a given cloud. The vertical dashed lines in the top row of Fig. 4, the log($N_{\rm H}$) PDFs, indicate each cloud's respective background $N_{\rm H}$ cut-off value, which were obtained from appendix B of Planck Collaboration XXXV (2016), are listed in Table 1, and represent our estimates of the average column density contribution from foreground and background dust. In addition to these plots, the median, geometric mean ($\mu_{\rm G}$), arithmetic mean standard deviation σ, and the geometric standard deviation are presented for $N_{\rm H}$ in Table 1, and for p and $\mathcal{S}$ in Table 2.

3.1.1 PDF of N_H

The PDFs in the top row of Fig. 4 show that there are clear differences in column density distribution among our targeted clouds. On the one hand, Corona Australis' and Chamaeleon-Musca's column densities are relatively low. In the case of Corona Australis, a large portion of the map's sightlines have $N_{\rm H}$ values that fall below the background reference value. On the other hand, Vela C, a young GMC, has a significantly higher $N_{\rm H}$ distribution and $\mu_{\rm G}(\log(N_{\rm H}))$ value than any other cloud. The Aquila Rift also has a particularly high $\mu_{\rm G}(\log(N_{\rm H}))$ value of 21.79, a value that is significantly above those of the other *Planck* clouds such as Cepheus, Ophiuchus, Lupus, Taurus, and Perseus (as can be seen in Table 1). It should once again be noted that the $N_{\rm H}$ PDFs were calculated before masking, and after being smoothed to a 15 arcmin FWHM resolution. These same trends can also be observed in Fig. 2, wherein each cloud's $N_{\rm H}$ map is presented with contours to represent $\log(N_{\rm H}/{\rm cm}^{-2}) = 21$ (*grey*), 21.5 (*black*), and 22 (*black*).

3.1.2 PDF of p

The polarization fraction PDFs show that Chamaeleon-Musca has particularly high polarization levels compared to the other clouds. Of our cloud sample, Vela C, Perseus, and the Aquila Rift show the lowest p value distributions (see Table 2). As discussed in Section 1, clouds with magnetic fields that are strong compared to turbulent gas motions will tend to have a high polarization fraction if the mean ordered magnetic field is not significantly inclined (King et al. 2018). However, there is a degeneracy with the viewing angle as the polarization fraction is roughly proportional to $\cos^2(\gamma)$, where γ is the averaged inclination angle between the magnetic field and the plane of the sky. Viewing the cloud along a sightline nearly parallel to the magnetic field will tend to result in very low measured polarization levels. It is likely that among our selected clouds there would be a range of viewing geometries and magnetic field strengths, resulting in a range of polarization fraction measurements.

The distribution of the polarization fraction p within a MC can also be used to estimate the average inclination angle of the magnetic field in the cloud, as described in Chen et al. (2019). For each of our Planck clouds, we first determined the maximum polarization fraction $p_{\rm max}$ within the cloud by examining the 1D PDF of p (see e.g. Fig. 4). Assuming this value corresponds to sightlines with uniform magnetic field (i.e. position angle $\psi =$ constant) completely on the plane of sky (i.e. inclination angle $\gamma = 0$) along the line of sight and considering the widely adopted dust polarization equations (see e.g. Fiege & Pudritz 2000):

$$q = \int n \cos 2\psi \cos^2\gamma \, {\rm d}z, \quad u = \int n \sin 2\psi \cos^2\gamma \, {\rm d}z,$$

$$p = p_0 \frac{\sqrt{q^2+u^2}}{N - p_0 N_2}, \quad N_2 = \int n \left(\cos^2\gamma - \frac{2}{3}\right) {\rm d}z, \tag{6}$$

one has

$$p_{\rm max} = \left.\frac{p_0 \cos^2\gamma}{1 - p_0\left(\cos^2\gamma - \frac{2}{3}\right)}\right|_{\cos^2\gamma=1} = \frac{p_0}{1 - \frac{1}{3}p_0}. \tag{7}$$

We then used equation (10) of Chen et al. (2019) to calculate the inclination angle $\gamma_{\rm obs}$ using the observed polarization fraction at each pixel, $p_{\rm obs}$:

$$\cos^2\gamma_{\rm obs} = \frac{p_{\rm obs}\left(1 + \frac{2}{3}p_0\right)}{p_0\left(1 + p_{\rm obs}\right)}. \tag{8}$$

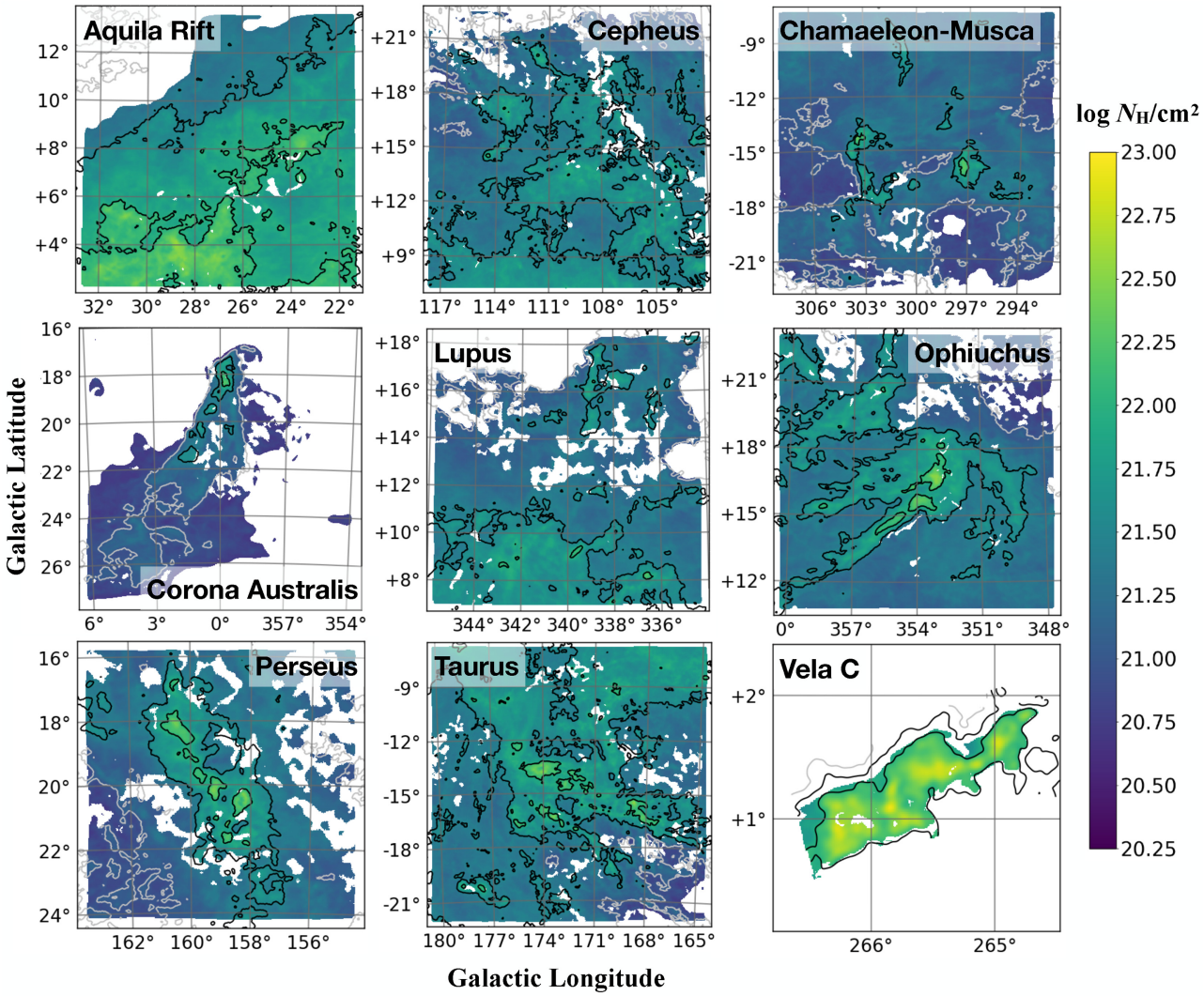

Figure 2. Maps of hydrogen column density (N_H), as obtained from *Planck* and BLASTPol observations, displayed in Galactic coordinates. These (N_H) maps from *Planck* were derived from a 353 GHz optical depth (τ_{353} GHz) map using equation (4), while the Vela C (N_H) map was derived from Herschel SPIRE and PACS submm maps. Each map has been masked according to the process described in Section 2.1, which entailed first smoothing the maps to 15 arcmin FWHM and then removing sightlines that contained values below a specific threshold. Each cloud's unique threshold value is presented in Table 1. Contours are shown for N_H, and the three contour levels are $\log(N_H/\mathrm{cm}^{-2}) = 21$ (*grey*), 21.5 (*black*), and 22 (*black*).

Following the methods of Chen et al. (2019), we consider the most probable value of $\gamma_{\rm obs}$ for all detections of $p_{\rm obs}$ among the entire cloud as the cloud-scale inclination angle of the magnetic field, $\hat{\gamma_{\rm obs}}$. We also adopted the $\mathcal{S}$-correction proposed in Chen et al. (2019) to include only regions that are less perturbed (with $\mathcal{S} < \langle\mathcal{S}\rangle$, the median value of $\mathcal{S}$), which tend to have smaller errors in p-derived inclination angle. The results are listed in Table 3, including the final estimate of the cloud-scale magnetic field inclination angle $\gamma_{\overline{B}}$ after considering the errors between the projected γ and the actual one in 3D (see the footnote of Table 3). We also note that, while there is no doubt that the value of $p_{\rm max}$ is influenced by the resolution of the polarization measurement (because larger telescope beams tend to remove extreme values of p; see e.g. King et al. 2018), as discussed in Chen et al. (2019), the uncertainty in determining $p_{\rm max}$ is unlikely to introduce large deviations in the derived inclination angle, and the projection effect from $\gamma_{\overline{B}}$ to $\gamma_{\rm obs}$ is relatively more significant. Because of this intrinsic error associated with projection from 3D to 2D, the expected accuracy of this method is only $\sim$10–30° (see discussions in Chen et al. 2019). Nevertheless, these values provide important input for our discussion on the properties of individual clouds in the next section.

3.1.3 *PDF of* $\mathcal{S}$

As for the $\mathcal{S}$ PDFs, we note that Chamaeleon-Musca and Perseus peak at the lowest and highest values of $\mathcal{S}$, with $\mu_{\rm G}(\mathcal{S}) = 3.8°$ and 11.13°, respectively. In contrast, Chamaeleon-Musca has the highest values of p, and the $\mu_{\rm G}(p)$ of Perseus is the second lowest, only slightly higher than that of Vela C. These results are consistent with previous observations of a negative correlation between p and $\mathcal{S}$ within individual clouds (Fissel et al. 2016; King et al. 2018; Planck Collaboration XII 2018). Other clouds also display a negative correlation between $\mathcal{S}$ and p distributions, but Chamaeleon-Musca and Perseus in particular display the strongest contrast. It is possible that these two clouds show such strong contrasts between p and $\mathcal{S}$ because they may be individual realizations of near-limiting cases: a

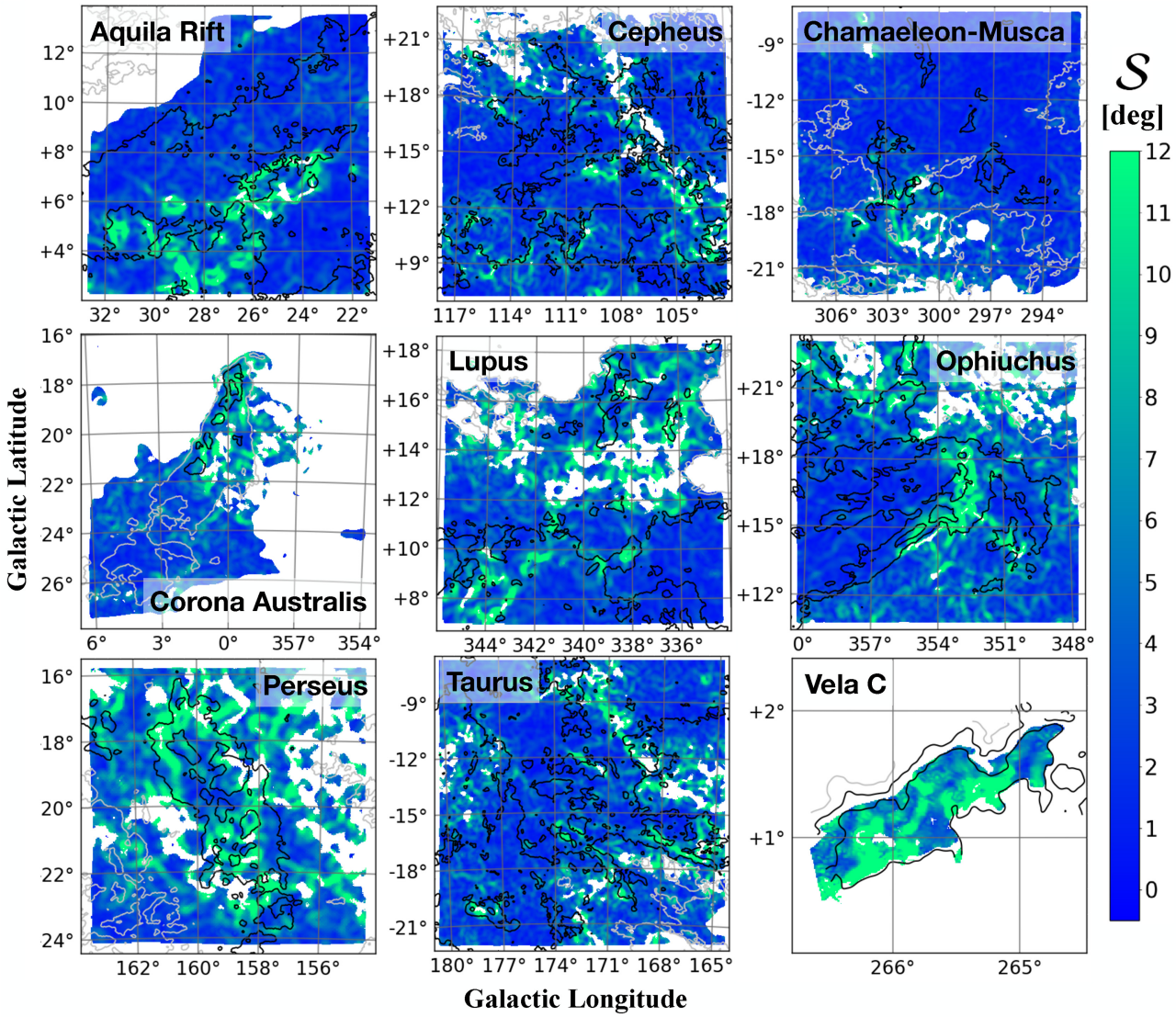

Figure 3. Maps of dispersion in polarization angles, as calculated using equation (2). Each map has been masked according to the process described in 2.1. Contours are shown for $N_{\rm H}$. The three contour levels are $\log(N_{\rm H}/{\rm cm}^{-2}) = 21$ (*grey*), 21.5 (*black*), and 22 (*black*).

large magnetic field strength and/or a low inclination angle in the case of Chamaeleon-Musca, and a weak field and/or a high inclination angle in the case of Perseus. Vela C is an outlier in the column density PDF, but it also has the lowest median p value, along with the second highest median $\mathcal{S}$ value among our sampled clouds. King et al. (2018) argued that this combination implies that Vela C has an unusually high inclination angle γ or potentially a weak magnetic field. These same trends can also be observed in Fig. 3, wherein each cloud's $\mathcal{S}$ map is presented with contours to represent where, within the cloud, $\log(N_{\rm H}/{\rm cm}^{-2}) = 21$ (*grey*), 21.5 (*black*), and 22 (*black*).

3.2 Joint correlations from 2D kernel density estimates

In this section, we examine the joint correlations between the polarization observables using KDE as described in King et al. (2018). For these comparisons, the *Planck* column density maps have been smoothed to the same 15 arcmin FWHM resolution as the p and $\mathcal{S}$ maps. The displayed slope values are calculated using the second eigenvector's x and y components, and the eigenvectors themselves are calculated using `numpy`'s linear algebra package in `Python`. These slopes thus represent the correlation between the different pairings of cloud observables. The results are presented in Fig. 5, with the fitted parameters listed in Table 4.

3.2.1 *The p–$\mathcal{S}$ correlation*

As previous studies have noted (see Planck Collaboration XIX 2015a; Planck Collaboration XX 2015b; Fissel et al. 2016; Planck Collaboration XII 2018), we find a negative correlation between $\log(p)$ and $\log(\mathcal{S})$ for all of our target clouds (bottom row of Fig. 5). The p versus $\mathcal{S}$ trend was first presented in Planck Collaboration XIX (2015a), and was based off of the distribution of p and $\mathcal{S}$ values from the entire sky. Planck Collaboration XX (2015b)'s found a similar correlation for higher resolution maps with observations restricted to $12^\circ \times 12^\circ$ fields of nearby clouds and diffuse ISM regions.

In comparing the p versus $\mathcal{S}$ trends among the various clouds, Vela C shows the steepest decrease in p with $\mathcal{S}$ compared to the other clouds (bottom row of Fig. 5). All of the clouds in our study have a negative p versus $\mathcal{S}$ slope, with a mean value of roughly -0.694,

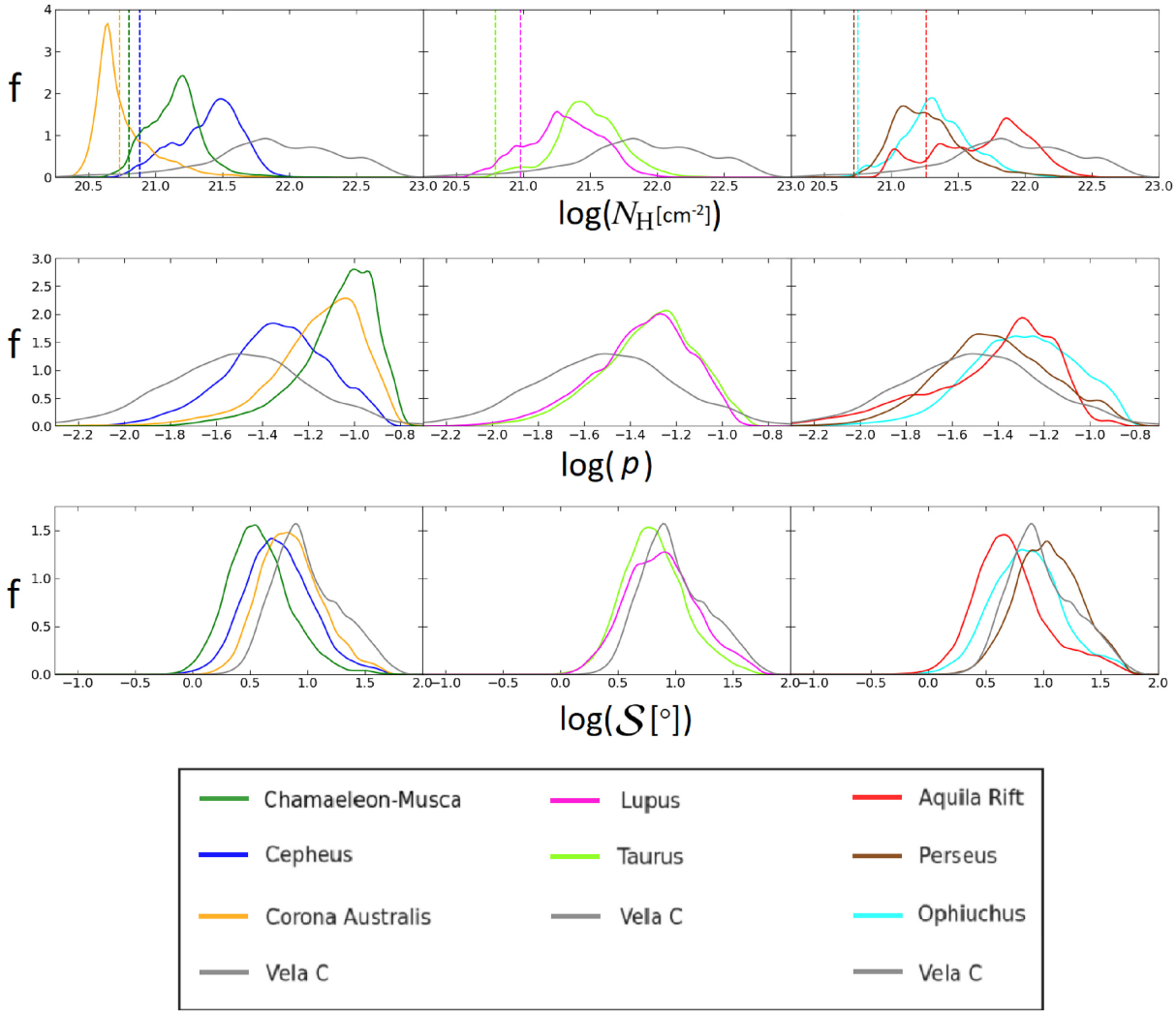

Figure 4. PDFs for each cloud's N_H (*top*), p (*middle*), and $\mathcal{S}$ (*bottom*) values on the smoothed scale of 15 arcmin FWHM. The y-axis in this figure shows the probability density, labelled here as f. Probability density is defined by the area under the curve which it creates: the probability of an x value being lower than a given quantity within the bounds of the curve is equal to the area under the curve to the left of that quantity. Each column displays the data from a specific subset of clouds, divided to increase the clarity of the plots. Vela C is shown in every plot as a reference for comparison. Note that the vertical dashed lines in the N_H PDFs indicate the column density threshold that each clouds sightline must be greater than to be included in our analysis, as displayed in Table 1 and discussed in Section 2.1. The column density N_H PDFs thus include all of each map's sightlines, however, only sightlines that passed the selection criteria described in Section 2.1 were used for the p and $\mathcal{S}$ PDFs shown in this figure.

while Vela C's p-$\mathcal{S}$ correlation has a slope of −0.930, though this may be partially caused by the narrower range of $\mathcal{S}$ in the Vela C polarization data. Studies of synthetic polarization observations by King et al. (2018) found that the inclination angle between the line of sight and mean magnetic field orientation of a cloud has a significant effect on the slope of its p versus $\mathcal{S}$ relationship. King et al. (2018), and later Chen et al. (2019), propose that the large p versus $\mathcal{S}$ slope of Vela C is caused by a large inclination angle of the mean magnetic field orientation with respect to the plane of the sky ($\sim 60°$). This is consistent with our findings in Section 3.1.2 where we used the method proposed in Chen et al. (2019) to estimate the inclination angle of the magnetic field for our clouds, and found that Vela C had an estimated mean cloud-scale magnetic field inclination angle of 56°.

Both Planck Collaboration XX (2015b) and Planck Collaboration XIX (2015a) argue that for large regions of the ISM where a wide range of magnetic field orientations are seen, the p versus $\mathcal{S}$ slope should be constant. While we agree that a negative correlation between p and $\mathcal{S}$ is certainly present in all of our target clouds, we find considerable variation in their p versus $\mathcal{S}$ slope values throughout our analysis, which appears to be significantly affected by the inclination angle of each cloud's magnetic field with respect to the plane of sky. We note that this variation in p versus $\mathcal{S}$ slopes seems to be correlated with inclination angles, as we have estimated lower inclination angles for the clouds with shallower slopes, and higher inclination angles for those that have steeper slopes (see Section 3.1.2 and Section 4).

The strength of this relationship may also be impacted by the sightline selection criteria that we have chosen to employ in Section 2.1. Although the *Planck* papers included polarization values from all sightlines, we have applied masks to our data to remove sightlines with low signal-to-noise polarization detections and where most of the emission is likely dominated by fore- or background diffuse dust. In doing so, however, we may somewhat bias our analysis towards

Table 3. Inclination angles of the cloud-scale magnetic fields derived from the distribution of polarization fraction, as described in Chen et al. (2019).

	$p_{\max}$	$\gamma^{\wedge}_{\rm obs}$	$\gamma^{\wedge}_{{\rm obs},S<\langle S\rangle}$	Estimated γ^{a}_{B}
AquilaRift	0.15	52.4°	51.2°	53°
Cepheus	0.16	56.5°	50.0°	51°
Chamaeleon-Musca	0.19	41.0°	35.1°	17°
Corona Australis	0.19	50.4°	44.3°	38°
Lupus	0.15	55.1°	48.9°	48°
Ophiuchus	0.16	58.3°	46.8°	43°
Perseus	0.18	62.8°	57.7°	68°
Taurus	0.15	52.0°	48.7°	48°
Vela C	0.14	63.9°	52.1°	56°

Notes. [a]As described in Chen et al. (2019), there are intrinsic differences between the observed inclination angle $\gamma_{\rm obs}$ derived from p and the actual inclination angle $\gamma_{\overline{B}}$ in the 3D space due to projection effects (see e.g. their figs 5 and 11). Here, we adopted the correlation between $\gamma^{\wedge}_{\rm obs}$ and $\gamma_{\overline{B}}$ shown in fig. 11 of Chen et al. (2019) to get the final estimate of the 3D inclination angle of the cloud-scale magnetic fields for the *Planck* clouds.

regions of higher polarization. which corresponds to regions of higher p and lower $\mathcal{S}$. As shown in Appendix A and Fig. A1, applying cuts to eliminate sightlines below the threshold column density tends to remove sightlines with high values of p and $\mathcal{S}$, while applying cuts based on P removes a larger number of low-p, high-$\mathcal{S}$ sightlines. Applying both selection criteria has the net effect of reducing the slope of the p versus $\mathcal{S}$ relation (see Fig. A4), but the relative ordering of the p-$\mathcal{S}$ slope indices remain largely unchanged (e.g. Chamaeleon-Musca/Perseus always have the shallowest/steepest slope regardless of which sightline selection criteria are used).

3.2.2 *The* p−$N_{\rm H}$ *correlation*

The column density–polarization fraction correlation has been reported in previous works to be robustly anticorrelated in a variety of targets (Planck Collaboration XIX 2015a; Fissel et al. 2016; King et al. 2018). In our sample, we find three clouds that do not follow this trend: Chamaeleon-Musca, Lupus, and Taurus (see the top row of Fig. 5). These clouds have very low statistical correlation between p and $N_{\rm H}$ (see Table 4). We note that for Chamaeleon-Musca there is very little range in polarization fraction, and the p values are systematically higher than those of other clouds.

The decreasing trend between p and $N_{\rm H}$ is usually explained by two processes: de-polarization due to changes in grain alignment efficiency or grain properties and the tangling of magnetic fields. As the $N_{\rm H}$ increases, an increasing number of dust grains that become shielded by other dust grains from the photons that have a short enough wavelength to exert radiative alignment torques. This means that p values may drop towards the high-$N_{\rm H}$ regions, as there are fewer dust grains that are aligned with respect to the local magnetic field and therefore the net polarization measured from the dust column is lower.

The correlation between polarization fraction p and hydrogen column density $N_{\rm H}$ has been studied in many previous polarization studies (e.g. Planck Collaboration XIX 2015a; Planck Collaboration XX 2015b; King et al. 2018; Planck Collaboration XII 2018). Among them, King et al. (2018) and Planck Collaboration XX (2015b) offer support in favour of two different interpretations of this anticorrelation. On the one hand, Planck Collaboration XX (2015b) argue that the whole sky trend is reproducible using synthetic observations assuming no variations in the efficiency of dust grain alignment with respect to the magnetic field. This implies that the observed depolarization is caused by magnetic field tangling within the telescope beam, i.e. the 3D geometry of the magnetic field. This appears to be consistent with the leading theory of grain alignment, radiative torque alignment (Lazarian & Cho 2005; Andersson et al. 2015), which demonstrated that large dust grains, specifically those found in MCs, can still be magnetically aligned in regions of high column density.

On the other hand, King et al. (2018) argued that the correlations obtained from synthetic observations of their MHD simulations, which did not include a loss of grain alignment efficiency towards high column density sightlines, could not reproduce the decrease in p observed with increasing $N_{\rm H}$ in Vela C. The efficiency with which grains are aligned nevertheless depends on the specific grain population in question, the microphysics of grain alignment, and properties of the local radiation field. King et al. (2018) argued that the lack of agreement between the p versus $N_{\rm H}$ trends found in Vela C and their simulations is primarily due to their assumption of homogeneous grain alignment. In King et al. (2019), it was further shown that by including a simple analytic model for the decrease in grain alignment efficiency with density, it is possible to reproduce the p versus $N_{\rm H}$ trends observed in the BLASTPol observations of Vela C.

There are two major differences between the work in King et al. (2018) and *Planck* studies that may contribute to the discrepancies. First, whereas King et al. (2018) evaluated the p−$N_{\rm H}$ slope using the entire p value distribution, Planck Collaboration XX (2015b) fitted the slope considering only the upper envelope of their p distributions, $p_{\max}$, to minimize the statistical impact of sightlines where the magnetic field orientation is significantly inclined from the plane of the sky, which decrease the observed polarization fraction. This is opposed to the fits of $\log(p)$ versus $\log(N_{\rm H})$ discussed in both this work and King et al. (2018).

In addition, as mentioned earlier, there is a significant difference in the range of column densities of the regions studied by Planck Collaboration XX (2015b) and our work. Most of the sightlines included in Planck Collaboration XX (2015b) trace the more diffuse component of the ISM, whereas our study includes only sightlines above a certain column density threshold, and are therefore more likely to include regions where radiative alignment torques are less efficient. Still, the discrepancy between the synthetic observations by King et al. (2018) and those presented in Planck Collaboration XX (2015b) warrants further study, and could point to a difference in the underlying physics of the simulation, e.g. the driving mechanism of turbulence. This discrepancy has important implications for interpreting polarization data. If the decrease in p versus $N_{\rm H}$ is only due to changes in dust grain alignment efficiency, the p versus $N_{\rm H}$ trend can be used to directly probe the dust physics. However, if the p versus $N_{\rm H}$ trend is also affected by the structure of the magnetic field, then it will be more difficult to model the grain alignment efficiency as a function of density.

3.2.3 *The* $\mathcal{S}$–$N_{\rm H}$ *correlation*

Based on the appearance of the $\mathcal{S}$ versus $N_{\rm H}$ KDE estimates, only a few clouds seem to show a weak positive correlation between $N_{\rm H}$ and $\mathcal{S}$ (see the middle row of Fig. 5). We therefore considered the Pearson and Spearman coefficients here, which are measurements of the level of correlation between two sets of data (see Table 4). In this case, they describe how likely it is that the observed slopes are actually caused by a statistical relationship between $\mathcal{S}$ and $N_{\rm H}$. The Pearson coefficient is a measure of linear correlation and the

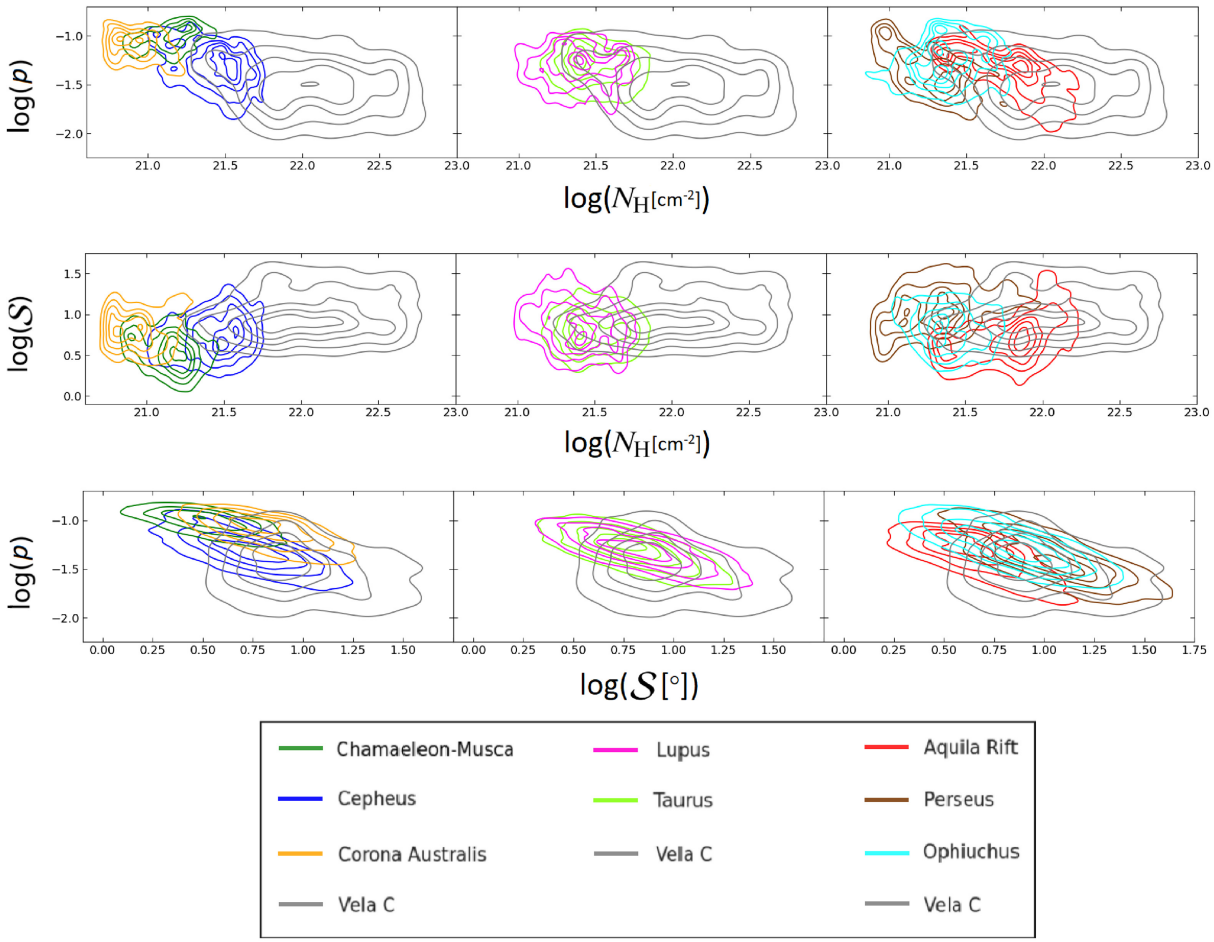

Figure 5. Joint PDFs of our polarization observables: *top row:* polarization fraction (p) versus hydrogen column density ($N_{\rm H}$), *middle row:* polarization angle dispersion ($\mathcal{S}$) versus $N_{\rm H}$, *bottom row:* p versus $\mathcal{S}$. Each contour colour represent a different molecular cloud, while the grey contours represent the data of the Vela C cloud, obtained from King et al. (2018) and provided in every plot as a point of comparison.

Table 4. This table shows the Pearson and Spearman coefficients for the correlations between each of the three sets of polarization comparisons: p-$N_{\rm H}$, $\mathcal{S}$-$N_{\rm H}$, and p-$\mathcal{S}$. The coefficients are denoted by P and an S subscripts, for Pearson and Spearman, respectively.

	$\rho_{{\rm P},p-N}$	$\rho_{{\rm S},p-N}$	$p-N$ index	$\rho_{{\rm P},\mathcal{S}-N}$	$\rho_{{\rm S},\mathcal{S}-N}$	$\mathcal{S}-N$ index	$\rho_{{\rm P},p-\mathcal{S}}$	$\rho_{{\rm S},p-\mathcal{S}}$	$p-\mathcal{S}$ index
AquilaRift	−0.670	−0.722	−1.12	0.452	0.459	1.60	−0.799	−0.732	−0.836
Cepheus	−0.342	−0.311	−0.702	0.202	0.193	4.40	−0.734	−0.718	−0.702
Chamaeleon-Musca	−0.005	0.182	−0.533	−0.071	0.139	−12.6	−0.714	−0.673	−0.533
Corona Australis	−0.627	−0.453	−0.687	0.352	0.212	2.00	−0.685	−0.670	−0.687
Lupus	−0.153	−0.123	−1.63	0.120	0.144	−7.69	−0.746	−0.742	−0.619
Ophiuchus	−0.077	−0.027	−1.23	0.022	−0.038	25.9	−0.762	−0.763	−0.708
Perseus	−0.594	−0.598	−0.882	0.272	0.285	1.20	−0.718	−0.719	−0.846
Taurus	−0.153	−0.156	−0.460	0.050	−0.039	5.50	−0.695	−0.676	−0.688
Vela C	−0.068	−0.055	−1.58	0.027	0.024	−3.89	−0.244	−0.249	−0.930

Spearman coefficient is a measure of monotonic correlation. For nearly all of our log($\mathcal{S}$) versus log($N_{\rm H}$) plots, both the Pearson and Spearman coefficient values had magnitudes that are close to zero ($|\rho_P|$, $|\rho_S| < 0.1$). This suggests that even though the data are consistent with a positive correlation, this correlation is very weak.

Overall, we were unable to establish a statistically robust relationship between $\mathcal{S}$ and $N_{\rm H}$. This lack of a measured correlation is in contrast to the results of Planck Collaboration XII (2018), which describe an observed trend of increasing $\mathcal{S}$ with increasing $N_{\rm H}$. The reason our data do not show this same correlation is likely a result of differences in the data samples. Planck Collaboration XII (2018) combined all of their *Planck* data and observed the average increase in $\mathcal{S}$ over a column density range of $1-20 \times 10^{21}$ cm^{-2}, whereas all of our $\mathcal{S}$ versus $N_{\rm H}$ analysis was done on a per-cloud basis. Among our sampled clouds, the average range of column density values was only within $0.98-11.0 \times 10^{21}$ cm^{-2}. In addition to our analyses covering a smaller range of column densities, the $\mathcal{S}$ versus $N_{\rm H}$ graph

upon which Planck Collaboration XII (2018)'s trend is based shows a region of little proportionality around the range of values in which our data generally falls. Therefore, this discrepancy in $\mathcal{S}$–$N_{\rm H}$ correlation may be due to the limited coverage in column density range in our analyses.

3.2.4 *Joint correlations from population statistic median value comparisons*

To cross-compare typical polarization values for all clouds, we plot the median values of p, $N_{\rm H}$, and $\mathcal{S}$ as functions of one another in Fig. 6. The horizontal and vertical bars show the median absolute deviation (MAD) for each cloud in order to indicate the typical spread of the variable.

Note that in these scatter plots, we have divided our Vela C sightlines into four different sub-regions as first defined in the *Herschel* imaging survey of OB young stellar objects' (HOBYS) study of Vela C (Hill et al. 2011). Two sub-regions, the CR and SR, show high column density filaments, while the CN and SN show extended lower column density filamentary structures at a variety of orientation angles. Of these sub-regions, the CR is the most active star-forming region and includes a compact H II region, powered by a cluster that contains an O9 star (Hill et al. 2011; Ellerbroek et al. 2013). It also has the highest polarization levels of all the sub-regions, and a high-density structure that is oriented strongly perpendicular to the magnetic field as well (Andersson et al. 2015; Soler et al. 2017; Jow et al. 2018).

We see that the decrease of p with increasing $N_{\rm H}$ and $\mathcal{S}$ observed within individual clouds is also seen in the comparison between median values for our sample of MCs. The presence of these trends on an intercloud scale, as opposed to a solely intracloud scale, suggests that these correlations between polarization quantities may be intrinsic, and not caused by cloud-specific properties or occurrences. Further investigation into this conclusion is left to future papers.

3.3 Relative orientation analysis

Another useful diagnostic of the magnetic field properties of a MC that is independent of our previous analysis is statistically comparing the orientation of the magnetic field to the orientation of cloud column density structures at every location on the map (histograms of relative orientation or HROs; Soler et al. 2013). In Planck Collaboration XXXV (2016), the authors showed that most of our sample clouds show a statistical change in alignment with respect to the magnetic field: lower column density sightlines have structures preferentially aligned with the magnetic field, while higher column density structures are more likely to have no preferred orientation or one that is perpendicular to the inferred magnetic field. When the relative orientation analysis was applied to RAMSES simulations in Soler et al. (2013), this change of relative orientation from parallel to perpendicular with increasing column density was only seen in high or intermediate magnetization simulations. Planck Collaboration XXXV (2016) therefore argued that most of the 10 nearby clouds in their study have the magnetic energy density equal to or larger than turbulence on cloud scales (see also Chen et al. 2016).

More recently, Jow et al. (2018) further quantified the relative orientation between magnetic field and gas structure using the projected Rayleigh statistics (PRS). In their analysis, Jow et al. (2018)

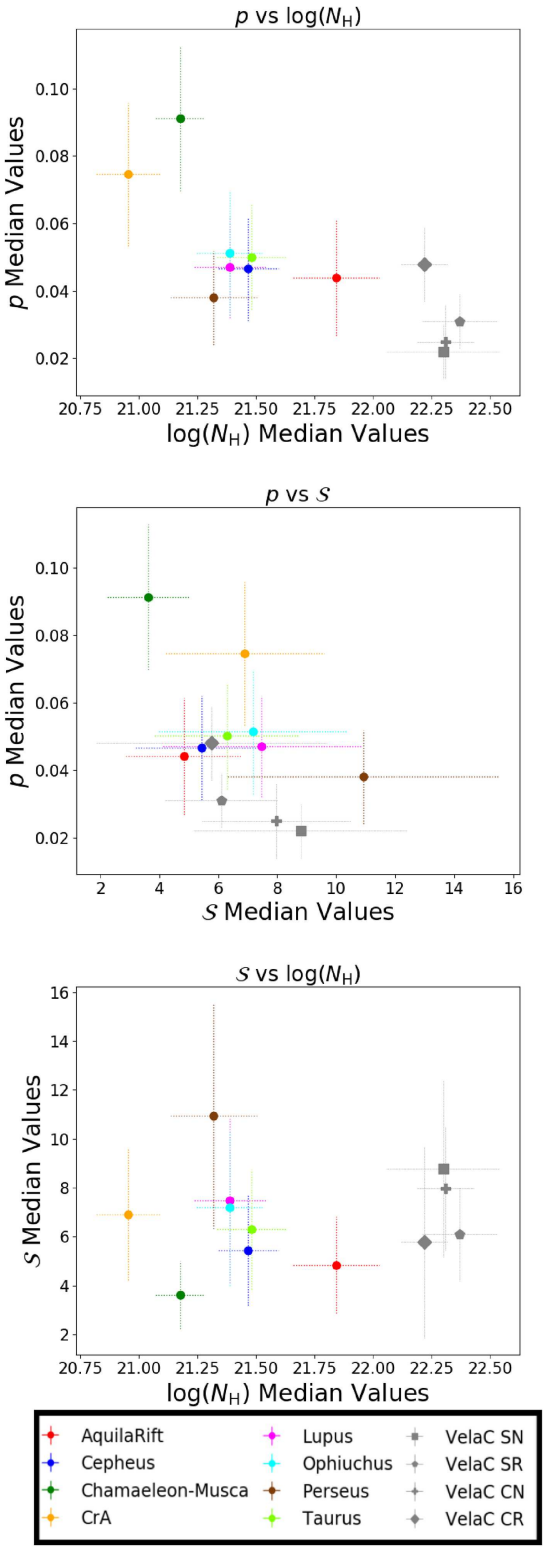

Figure 6. A set of plots comparing the median values of the three main polarization properties of our target clouds: polarization fraction (p), dispersion in polarization angles ($\mathcal{S}$), and the logarithm of hydrogen column density ($\log N_{\rm H}$). The horizontal and vertical dotted lines represent the median absolute deviation (MAD), which roughly indicates the distributions of each quantity. The dotted error bars are used to represent MADs all throughout this paper. Here, Vela C is broken into four sub-regions: South-Nest (SN), South-Ridge (SR), Centre-Nest (CN), and Centre-Ridge (CR).

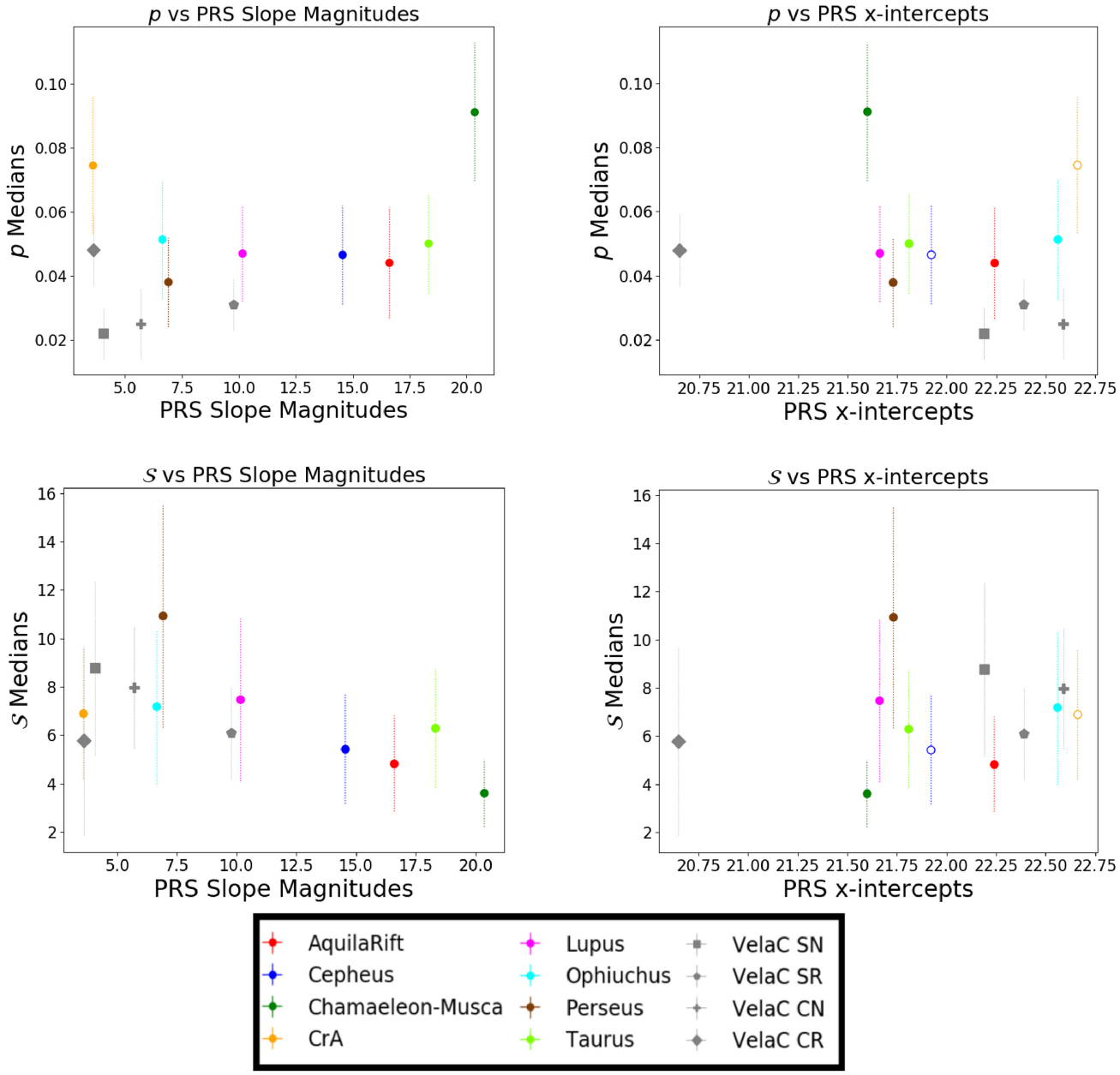

Figure 7. A series of scatter plots comparing the median p and $\mathcal{S}$ values from our study to the slope and x-intercept values of the PRS plots, as determined by the study Jow et al. (2018). Vertical bars are again used to present each quantity's median absolute deviation (MAD). We were unable to create similar error bars for the PRS slope or x-intercept values, as we could not obtain any associated errors from Jow et al. (2018). PRS values for Vela C as a whole were not obtainable as analysis of the total cloud was not conducted in the study. We therefore present one data point for each sub-region of the GMC: the South-Ridge (SR), South-Nest (SN), Centre-Ridge (CR), and Centre-Nest (CN). The open circles indicate that the transition from positive to negative PRS was not observed by Jow et al. (2018), so the x-intercept was extrapolated from the linear fit.

calculated the PRS using the following equation:

$$Z_x = \frac{\sum_i^n \cos\theta_i}{\sqrt{n/2}}, \tag{9}$$

where Z_x is the PRS, and $\theta_i = 2\phi_i$ for which $\phi_i \in [-\frac{\pi}{2}, \frac{\pi}{2}]$, where ϕ is the relative angle between the polarization orientation and $N_{\rm H}$ gradient orientation at each point. The sign of Z_x in this application corresponds to different relative orientations of a cloud's magnetic field with respect to its column density gradients: $Z_x > 0$ indicates that the column density contours are preferentially oriented parallel to the magnetic field; $Z_x < 0$ instead indicates that the column density contours are preferentially oriented perpendicular to the magnetic field lines. $Z_x \approx 0$ represents a complete lack of measured preferential alignment between the two. Jow et al. (2018) also fit a linear trend to Z_x versus $\log(N_{\rm H})$ and reported, using the BLASTPol data of Vela C, that the PRS slope value and $N_{\rm H}$ intercept can be used to attempt to analyse the alignment between the magnetic field and column density variations.

Using the measured PRS slope magnitudes and $N_{\rm H}$ intercepts of the *Planck* clouds provided in Jow et al. (2018), we plotted the correlation between the PRS measurements and the observed polarimetric properties in Fig. 7. Though a large slope often correlates

with a more rapid shift in preferential alignment from parallel to perpendicular with increasing $N_{\rm H}$ (thus a more ordered and stronger magnetic field), note however that the maximum amplitude of Z_x is proportional to n (particularly in the high-n limit), where n is the number of independent measurements of θ_i. Therefore, a cloud such as Corona-Australis, which has relatively few sightlines, will tend to show a lower range in Z_x values, and thus a shallower slope compared to clouds with more sightlines.

Nevertheless, we find a particularly noticeable trend in the $\mathcal{S}$ versus PRS slope magnitudes plot (Fig. 7, bottom left). There seems to be a negative relationship between the dispersion in polarization angle $\mathcal{S}$ and the magnitude of slopes from linearly fitting the PRS Z_x versus $\log(N_{\rm H})$ correlation. In short, large slope values tend to be observed in clouds with low average disorder in the projected magnetic field orientation, while small slope values are more often seen in clouds with more disordered magnetic fields (see more discussions in Jow et al. 2018).

This could be interpreted as both the $\mathcal{S}$ and PRS slope measurements being influenced by the magnetic field strength and inclination angle of the clouds. A strong magnetic field will resist turbulent gas motions perpendicular to the magnetic field direction, and thus maintain a more ordered magnetic field orientation (lower $\mathcal{S}$), as opposed to a weak magnetic field in which turbulent gas motions will more easily be able to alter the magnetic field geometry (higher $\mathcal{S}$). Weak magnetic fields leading to a more disordered field geometry results in a lower degree of alignment with the cloud column density structure, and therefore lower magnitude PRS values.

Inclination angle of the magnetic field with respect to the plane of sky is another important factor in this relationship between $\mathcal{S}$ and PRS slopes, as it has a significant influence on each observable. As discussed in Section 3.1, a high inclination angle of the mean magnetic field will result in a high $\mathcal{S}$ value due to projection effects. This same exaggeration of the apparent magnetic disorder leads to a decrease in PRS slope magnitudes. In cases where the mean magnetic field is significantly inclined with respect to the plane of the sky, small variations in the magnetic field orientation caused by turbulence can result in large differences in projected magnetic field orientation. More disorder in the projected magnetic field orientation can result in less correlation with the orientation of cloud column density structure, thus creating a much weaker and more shallow Z_x versus $N_{\rm H}$ trend. Soler et al. (2013) also showed that in the rare case where the magnetic field is parallel to the line of sight, no preferential orientation with respect to column density can be seen.

To explore this trend further, we calculated the Pearson and Spearman coefficients of the median $\mathcal{S}$ versus PRS slope relationship. The result was a Pearson coefficient of -0.771 and a Spearman coefficient of -0.741, which suggests that these variables are correlated. Further analysis into the significance of this trend would be a valuable area of study.

As shown in Jow et al. (2018), the values of Z_x transition from positive to negative in the PRS plot for all but two clouds; this transition corresponds to a change in relative orientation from being preferentially parallel to preferentially perpendicular. The PRS x-intercept is a crude estimate of point at which this change occurs, and is based on the assumption that Z_x and $N_{\rm H}$ share a linear relationship. Instead of x-intercepts naturally occurring within their PRS plots, Cepheus and Corona Australis had to have their the x-intercepts extrapolated from the linear fit (see fig. A1 of Jow et al. 2018). These extrapolated values are indicated by the hollow data points in Fig. 7. It has been suggested that this transition point signifies a shift in relative strength between gas kinetic energy density and magnetic energy density, which suggests a transition between being sub-Alfvénic and being super-Alfvénic (also see e.g. Chen et al. 2016). The PRS plots from Jow et al. (2018) seem to suggest that nearly all of the clouds in our sample thus fall into the categorization of trans-Alfvénic or sub-Alfvénic.

4 COMPARISON WITH SYNTHETIC POLARIZATION OBSERVATIONS

In Section 3.2, it was noted that Vela C had a strong negative correlation between its p and $\mathcal{S}$ quantities. King et al. (2018) attempted to explain this correlation in Vela C by comparing the observed polarization distributions to the polarization distributions of synthetic polarization maps made from 3D MHD simulations. In these simulations, MCs are formed from the collision of two convergent gas flows, which creates a dense post-shock gas layer wherein filaments and cores form (Chen & Ostriker 2014, 2015). Due to shock compression, the magnetic fields in these sheet-like clouds roughly align with the post-shock layer. Two simulations were examined: Models A and B. In Model A, the cloud formed in the post-shock region is relatively more turbulent and has higher turbulent-to-magnetic energy ratio, with an average Alfvén Mach number $\mathcal{M}_{A,\rm ps} \approx 2.43$. In contrast, Model B was originally designed to simulate a local star-forming region within a magnetically supported cloud (see Chen & Ostriker 2014, 2015), and thus has well-ordered magnetic field structure with less-perturbed gas ($\mathcal{M}_{A,\rm ps} \approx 0.81$). These simulated clouds were 'observed' at a variety of viewing angles with respect to the post-shock layer, and the only synthetic observations of these clouds that had similar p-$\mathcal{S}$ slopes to Vela C were those with large inclination angles of the magnetic fields with respect to the plane of sky ($\gamma \gtrsim 60^\circ$ for Model A and $\gamma \gtrsim 75^\circ$ for Model B).

Here, we compare the polarization properties of nine clouds to the simulations presented in King et al. (2018). This allows us to better characterize the physical properties of the *Planck* clouds by directly comparing them with these synthetic observations and determining which synthetic observations (simulation models and viewing angles) can best reproduce the observed polarization properties within the clouds. This process also helps to validate the results of King et al. (2018) by showing that the simulated observations share similarities with a larger variety of clouds than just Vela C.

We note that $\mathcal{S}$ is a more useful quantity for comparisons than p, because King et al. (2018) assumed uniform grain alignment and a prescribed coefficient of polarization fraction (p_0) of 0.15. In fact, more recent work by King et al. (2019) showed that the p versus $N_{\rm H}$ correlations can be strongly affected by non-homogeneous grain alignment efficiency in higher column density regions; without a microphysically accurate grain alignment efficiency model, using this correlation to establish magnetic field properties of the target is a difficult proposition. The p versus $\mathcal{S}$ correlations, however, show very little dependence on polarization efficiency assumptions (King et al. 2019). The mean $\mathcal{S}$ values and the p-$\mathcal{S}$ correlation power-law index can therefore be considered to better reflect the magnetic properties of the clouds.

Fig. 8 shows a scatter plot of the p-$\mathcal{S}$ logarithmic slopes (power-law indices; see Table 4) and the mean $\mathcal{S}$ values [$\mu_{\rm G}(\mathcal{S})$; see Table 2] for all of the *Planck* clouds considered in this study, Vela C, and synthetic observations of the two models discussed in King et al. (2018) viewed from different inclination angles with respect to the mean magnetic field direction in the post-shock layer. We note that the synthetic polarization observations adopted here were analysed at the full pixel-scale resolution of the simulations reported in King

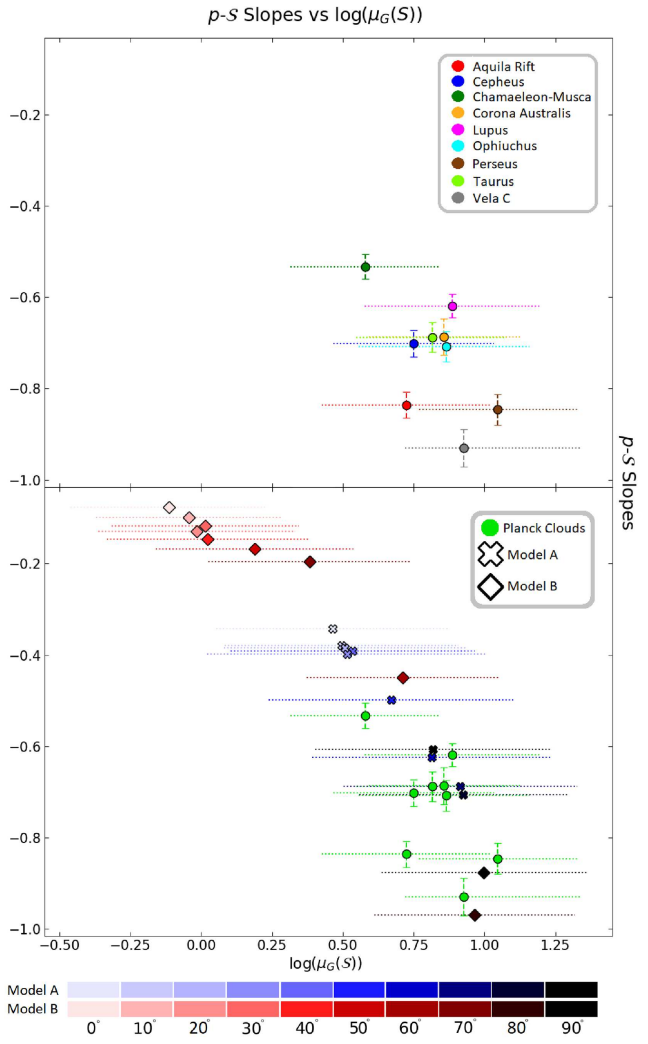

Figure 8. Correspondence between the slope of a cloud's p versus $\mathcal{S}$ relationship and the geometric mean of $\mathcal{S}$ (in log scale), for both observed data (*top and bottom panels*) and those measured from synthetic observations (King et al. 2018; *bottom panel*) of a more turbulent cloud (Model A; *thick plus*) and a more magnetically dominated cloud (Model B; *diamonds*). The average magnetic field inclination angles for the synthetic observations are represented by the colour map depicted beneath the plot, with the inclination angle increasing from 0° to 90° in 10° intervals. The dotted horizontal lines on the x-axis show the MAD of each cloud's $\mathcal{S}$ values and are thus a representation of the distribution of $\mathcal{S}$-values. The error bars on the y-axis represent 3σ confidence intervals of slope values obtained from bootstrap estimates.

et al. (2018), which is significantly higher than the 0.6–2.1 pc o*Planck* and BLASTPol maps of this study. However, King et al. (2018) found that the polarization distributions were not significantly affected by resolution, and we have verified with the 0.5 pc resolution synthetic observations available from their study that the locations of the p-$\mathcal{S}$ versus mean $\mathcal{S}$ model points are not significantly affected by resolution. Also note that, King et al. (2018) considered the *rotation angle* of the simulation box as the analysis parameter, however, there are intrinsic angles of the average magnetic field relative to the shocked layer and thus the rotation axis (see e.g. Chen et al. 2019). Here, we incorporated the intrinsic inclination angles of the cloud-scale magnetic field as measured in Chen et al. (2019) when varying the viewing angles of the synthetic observations, and thus the angles shown in Fig. 8 represent the actual angle between the average magnetic field and the plane of sky. For the *Planck*/BLASTPol data, we have also attempted to estimate the uncertainty in our measurement of the p-$\mathcal{S}$ slope, through bootstrap errors. These bootstrap estimates were obtained by calculating the slope of each cloud 1000 times, with each slope estimated from a random sample of 25 000 sightlines.

We first note that our sample of clouds are not well matched by the synthetic polarization observations of the strong-field simulation, Model B. In order to match the mean $\mathcal{S}$ values of the observations with Model B, we would infer that the mean magnetic field direction is nearly aligned with the line of sight for 8 of 9 clouds, which is not very likely. In addition, Model B predicts shallow slopes (less negative power-law indices) in the log (p) versus log (S) plots when viewed from low-inclination lines of sight, which are not consistent with the slopes measured in our clouds. We therefore conclude that, in general, these nearby MCs are not consistent with simulated clouds that have a highly ordered magnetic field.

In contrast, Model A, the more turbulent cloud, can generally reproduce the mean $\mathcal{S}$ values, and can better reproduce the p-$\mathcal{S}$ slopes for all clouds without requiring a single, shared magnetic field orientation for all clouds. Most clouds are consistent with synthetic observations with reasonable inclination angles ($\gamma \gtrsim 40°$) of the magnetic field. The exceptions to this are Perseus, Vela C, and the Aquila Rift, which appear to have a steeper p-$\mathcal{S}$ slope correlation than predicted from Model A. We note that, as demonstrated in King et al. (2018) and discussed in Section 3.1.2, the p-$\mathcal{S}$ slope itself could be correlated with the cloud-scale magnetic field orientations with respect to the line of sight, which has a strong impact on the level of polarization fraction (see e.g. Chen et al. 2019). This indicates that the results shown in Fig. 8 could be dependent on different methods for cloud sightline selection, as discussed in Appendix A. Nevertheless, all the different sightline masking methods we tested (see Appendix A) show better agreement with Model A than Model B for the observations. Indeed, a more detailed analysis with synthetic observations that mimic the effect of sightline masking is needed to use the p-$\mathcal{S}$ slope to infer the mean magnetic field inclination angle. This is beyond the scope of this paper.

Among the observed clouds, Chamaeleon-Musca is the only one that could potentially be consistent with the magnetically dominated Model B without requiring an unreasonably high inclination angle ($\gamma \gtrsim 75°$) of the magnetic field. This is in fact the cloud with the highest polarization fraction in our analysis (see Table 2 and Figs 4 and 6). This lends credit to the idea that Chamaeleon-Musca may have a relatively strong cloud-scale magnetic field compared to the other clouds in this study.

Overall, our cloud polarization observation data in Fig. 8 better match the synthetic observations of a turbulent cloud that is not dynamically dominated by magnetic field (Model A in King et al. 2018). The better agreement with the more turbulent, super-Alfvénic Model A, would seem to conflict with the conclusions of the PRS analysis (Jow et al. 2018) discussed in Section 3.3, where the measured transition in relative gas-field orientation was taken to indicate that the gas must be trans- or sub-Alfvénic at cloud scale. However, we note that the Alfvén Mach number of Model A cited from King et al. (2018), $\mathcal{M}_{\rm A} \approx 2.5$, is an average value among the entire cloud, and thus should not be taken as a diagnostic of all local gas conditions. King et al. (2018) also did not consider the gas flow direction with respect to the magnetic field when calculating $\mathcal{M}_{\rm A}$. In fact, the value of $\mathcal{M}_{\rm A}$ would be reduced if only the velocity component perpendicular to local magnetic field is considered. Under this definition, the simulated cloud in Model A

of King et al. (2018) is indeed trans-Alfvénic (see also Chen et al. 2019 for more discussions). We would also like to point out that the derived Alfvén Mach numbers within individual clouds should only be considered as references, not definitive properties of the entire clouds. In fact, since MCs are spatially large and likely cover a wide range of physical environments, it is inappropriate to use a single value to represent the properties of the entire cloud.

5 CONCLUSIONS

The goal of this study was to characterize the magnetic field properties of nine nearby MCs. This characterization was done by comparing 353 GHz polarization data of eight clouds from the *Planck* survey and 500 μm polarization data on Vela C from BLASTPol, and investigating polarization observables such as polarization fraction (p) and the local dispersion in polarization angles ($\mathcal{S}$). We also examine the correlation of these polarization properties with *Planck* hydrogen column density maps of our target regions. Comparisons were drawn between our observations and those of Planck Collaboration XX (2015b), Planck Collaboration XII (2018), and Planck Collaboration XXXV (2016) in particular. We also compare our observations to synthetic polarization observations of two simulations from King et al. (2018): Model A, a more turbulent simulation where the energy density in the magnetic field is comparable to the energy density of turbulent gas motions, and Model B, a simulation where the magnetic energy density dominates turbulence with a very ordered magnetic field. The main conclusions of our paper are as follows:

(1) Using the methods described in Chen et al. (2019), we estimate the average inclination angle of each cloud's magnetic field. This process is based on each cloud's maximum polarization fraction value ($p_{\rm max}$) and the 1D probability distribution function of p that are shown in Fig. 4. The estimated inclination angles that we obtained are presented in Table 3, and range from 17° to 68°.

(2) In King et al. (2018), it is suggested that the slope of a cloud's p versus $\mathcal{S}$ relationship is strongly affected by the inclination angle of the cloud's magnetic field with respect to the plane of sky. We were able to provide support for this assertion in Fig. 8 by plotting each cloud's p versus $\mathcal{S}$ slope, including the values for King et al. (2018)'s Models A and B at 10° increments between 0°and 90°, against its geometric mean $\mathcal{S}$ value [$\mu_{\rm G}(\mathcal{S})$]. We find an increase in p versus $\mathcal{S}$ slope magnitude with increases in $\mathcal{S}$, which is in turn correlated with increases in inclination angle (see Section 3.1.2). This suggests that as magnetic fields become more apparently disordered, by either a decrease in field strength or an increase in inclination angle, the rate at which p will vary with respect to $\mathcal{S}$ increases.

(3) In most of our cloud sample, we observe a systematic trend of decreases in p with increases in $N_{\rm H}$. This trend is present both within and between clouds, with the exception: Chamaeleon-Musca, Lupus, and Taurus. These clouds do not show strong correlations between p and $N_{\rm H}$, as evidenced by their very low Pearson and Spearman coefficients as well as Chamaeleon-Musca's low slope value and extremely low Pearson and Spearman coefficients. It is possible that the difference lies in their narrow $N_{\rm H}$ distributions. We also note that these clouds have fairly low median $N_{\rm H}$ values. The small range of $N_{\rm H}$ values in these clouds may not be providing a wide enough range of values for a significant trend to be observed. In their analysis, King et al. (2018) compared the p versus $N_{\rm H}$ slopes from their synthetic polarization observations of two different colliding flow simulations with that of their Vela C BLASTPol observation, and they found that their simulations were unable to accurately recreate the observed drop in p versus $N_{\rm H}$. We compare our observed slope values and find the same result: neither Model A nor Model B has a p versus $N_{\rm H}$ relationship that resembles those derived from the *Planck* or BLASTPol data.

(4) We were unable to establish a statistically significant relationship between hydrogen column density ($N_{\rm H}$) and dispersion in polarization angles ($\mathcal{S}$). Although nearly all eigenvalue slopes produced by our covariance matrices showed the predicted positive trend, their associated Pearson and Spearman coefficients were incredibly low (Table 4), and thus the trend is not statistically significant. Planck Collaboration XII et al. (2018) reported a trend of increasing $\mathcal{S}$ with $N_{\rm H}$, but we were not able to confirm its existence with the analytical methods used in this work.

(5) A negative correlation between dispersion in polarization angles ($\mathcal{S}$) and the magnitude of PRSc (PRS) slope magnitudes has been observed for all clouds. The statistical relevance of this correlation has been evaluated through the use of Pearson and Spearman coefficients, and it is found to be significant. We believe that this relationship is caused by the two variables' individual dependencies on both magnetic field strength and viewing geometry, and may be useful in future attempts to determine the inclination angle and relative energetic importance of the magnetic field versus turbulent gas motions within MCs.

(6) Among the clouds observed, Chamaeleon-Musca shows the highest p values, the lowest $\mathcal{S}$ values, and the shallowest p versus $\mathcal{S}$ slope magnitude. Chamaeleon-Musca is also the only cloud with p-$\mathcal{S}$ slope and mean ($\mathcal{S}$) values that are consistent with those of King et al. (2018)'s strongly magnetized MC simulation, Model B. This could imply that the magnetic field in Chamaeleon-Musca is more ordered, and possibly more dynamically significant, than the magnetic fields in other MCs considered in this study. However, the estimated inclination angle with respect to the plane of the sky of the cloud-scale magnetic field in Chamaeleon-Musca is ≈17°, which is the lowest of all clouds in our sample. A low inclination angle of the mean magnetic field would also result in low $\mathcal{S}$ values and a shallow p-$\mathcal{S}$ slope, and so with these observations alone we can not conclusively state that Chamaeleon-Musca has a stronger magnetic field than the other clouds in our sample.

It is our intent that these data be used for future research on the effects that magnetic fields have on star formation. For future analysis of these clouds, their polarization parameters, and the relation of these results to rates of star formation, we suggest that clouds such as Perseus be broken down into their sub-regions, as we have done for Vela C in parts of this paper. Our whole-cloud analysis over-simplifies the complicated magnetic field morphology of these MCs and assumes that the inclination angle of the magnetic field is more or less constant across each map. In addition, future synthetic observations should attempt to replicate the biases associated with sightline selections, and polarized background and foreground emission. These selections affect the precise values of the average properties and correlations of polarization measurements. Future work would also benefit from analyses using more tracers of magnetic field properties, including observations of background stars in optical or near-infrared bands, Faraday rotation, and Zeeman splitting. To further understand the observational biases towards highly polarized regions that is caused by polarization intensity-based sightline selection criteria, it would be helpful to apply a similar selection criteria to synthetic polarization maps by masking regions of low polarization intensity. This simulation masking may help to determine how these sightline selection criteria affect their resulting polarization distributions.

ACKNOWLEDGEMENTS

This work was supported by the University of Virginia and the National Radio Astronomy Observatory, including its funders (Associated Universities Inc. and the National Science Foundation). This research used ASTROPY,[2] a community-developed core PYTHON package for Astronomy (Astropy Collaboration 2013; Price-Whelan et al. 2018). CHS acknowledges partial summer support from the University of Virginia through the Virginia Initiative on Cosmic Origins. LMF, CYC, and ZYL are supported in part by the National Science Foundation AST-1815784. LMF and ZYL acknowledge support from the National Aeronautics and Space Administration 80NSSC18K0481. ZYL is supported in part by the National Aeronautics and Space Administration 80NSSC18K1095 and the National Science Foundation AST-1716259 and 1910106. This work has been partially supported by the National Aeronautics and Space Administration as part of the Balloon-borne Large-Aperture Submillimeter Telescope (BLAST) experiment, under award numbers NNX13AE50G and 80NSSC18K0481. PKK is supported by a Livermore Graduate Scholarship at Lawrence Livermore National Laboratory, and acknowledges the Jefferson Scholars Foundation for additional support through a graduate fellowship. Part of this work was performed under the auspices of the Department of Energy by Lawrence Livermore National Laboratory under Contract DE-AC52-07NA27344. LLNL-JRNL-785178. CHS was a summer student at the National Radio Astronomy Observatory. LMF was supported by a Jansky Fellowship from the National Radio Astronomy Observatory and also by funding from the Natural Sciences and Engineering Research Council of Canada (NSERC).

DATA AVAILABILITY

No new data were created or analysed as part of this research. The simulation data underlying this article will be shared on reasonable request to P. K. King and/or C.-Y Chen.

REFERENCES

Andersson B. G., Lazarian A., Vaillancourt J. E., 2015, ARA&A, 53, 501
Astropy Collaboration, 2013, A&A, 558, A33
Chen C.-Y., Ostriker E. C., 2014, ApJ, 785, 69
Chen C.-Y., Ostriker E. C., 2015, ApJ, 810, 126
Chen C.-Y., King P. K., Li Z.-Y., 2016, ApJ, 829, 84
Chen C.-Y., King P. K., Li Z.-Y., Fissel L. M., Mazzei R. R., 2019, MNRAS, 485, 3499
Crutcher R. M., 2012, ARA&A, 50, 29
Ellerbroek L. E. et al., 2013, A&A, 558, A102
Fiege J. D., Pudritz R. E., 2000, ApJ, 544, 830
Fissel L. M. et al., 2016, ApJ, 824, 134
Fissel L. M. et al., 2019, ApJ, 878, 110
Galitzki N. et al., 2014, in Stepp L. M., Gilmozzi R., Hall H. J., eds, Proc.SPIE. Conf. Ser. Society of Photo-Optical Instrumentation Engineers (SPIE) Conference Series, Vol. 9145. SPIE, Bellingham, WA, USA, p. 91450R
Hildebrand R. H., 1988, QJRAS, 29, 327
Hill T. et al., 2011, A&A, 533, A94
Jow D. L., Hill R., Scott D., Soler J. D., Martin P. G., Devlin M. J., Fissel L. M., Poidevin F., 2018, MNRAS, 474, 1018
King P. K., Fissel L. M., Chen C.-Y., Li Z.-Y., 2018, MNRAS, 474, 5122
King P. K., Chen C.-Y., Fissel L. M., Li Z.-Y., 2019, MNRAS, 490, 2760
Lazarian A., Cho J., 2005, in Adamson A., Aspin C., Davis C., Fujiyoshi T., eds, ASP Conf. Ser., Vol. 343, Astronomical Polarimetry: Current Status and Future Directions. Astron. Soc. Pac., San Fransisco, p. 333
McKee C. F., Ostriker E. C., 2007, ARA&A, 45, 565
Planck Collaboration XI, 2014, A&A, 571, A11
Planck Collaboration XIX, 2015a, A&A, 576, A104
Planck Collaboration XX, 2015b, A&A, 576, A105
Planck Collaboration XXXV, 2016, A&A, 586, A138
Planck Collaboration XII, 2020, A&A, 641, A12
Price-Whelan A. M. et al., 2018, AJ, 156, 123
Soler J. D., Hennebelle P., Martin P. G., Miville-Deschênes M. A., Netterfield C. B., Fissel L. M., 2013, ApJ, 774, 128
Soler J. D. et al., 2017, A&A, 603, A64
Soler J. D., Bracco A., Pon A., 2018, A&A, 609, L3
Yamaguchi N., Mizuno N., Saito H., Matsunaga K., Mizuno A., Ogawa H., Fukui Y., 1999, in Nakamoto T., ed., Star Formation. Nobeyama Radio Observatory, Japan, p. 80
Zucker C., Speagle J. S., Schlafly E. F., Green G. M., Finkbeiner D. P., Goodman A. A., Alves J., 2019, ApJ, 879, 125

[2]http://www.astropy.org

APPENDIX A: DISCUSSION OF *PLANCK* SIGHTLINE SELECTION BIASES

In analysing polarization data in this paper, we have only included sightlines above a column density threshold characteristic of the diffuse ISM at the same Galactic latitude, and required that the polarized intensity P be at least 3× larger than the associated uncertainty ($P \geq 3\sigma_P$) in the *Planck* maps (see Section 2.1 for more details). The goal of the column density masking threshold is to only analyse sightlines that are above the typical diffuse ISM background column density, and therefore likely associated with the cloud. The goal of the polarization selection criteria is to only analyse polarization data that has a high degree of statistical significance, and therefore does not require complicated error debiasing analysis as discussed in Planck Collaboration XIX (2015). However, it is important to examine whether these selection criteria bias our fits of the relationships between polarization measureables by rejecting regions of the cloud where the polarization is weak.

In Figs A1 and A2, we examine the distribution of p versus $\mathcal{S}$ points for the Taurus, Perseus, and Aquila maps using four different masking methods. In the leftmost panel, the distribution of all sightlines with no masking shows more points at low p and high $\mathcal{S}$ as well as more points at high p and high $\mathcal{S}$ compared to the third column, which shows the sightlines for the masking criteria used in the main paper text. The high p and high $\mathcal{S}$ sightlines are absent in the second column, where we removed sightlines where the column density $N_{\rm H}$ is less than the mean column density in a diffuse ISM region at the same Galactic latitude. This is not surprising, as low column density sightlines tend to have higher polarization fractions for the same values of p and $\mathcal{S}$ (Fissel et al. 2016). Masking these diffuse sightlines has the effect of making the correlation between $\log(p)$ and $\mathcal{S}$ closer to a linear trend.

When we apply the second criteria for selecting the sightlines used in the main paper text, that the polarized intensity P be at least 3× larger than the σ_P, we find that this removes the lowes p values in the plots, which tend to have high $\mathcal{S}$-values. Detections of polarization below this level are not statistically significant, but this does bias our data slightly towards lower average polarization angle dispersion $\mathcal{S}$, and higher average fractional polarization values p.

To be fully consistent with Planck Collaboration XXXV (2016), which used the same Planck maps as this study but at 10 arcmin FWHM resolution instead of 15 arcmin FWHM resolution, we would have to apply one additional sightline selection criteria. This selection criteria would require that the polarized radiation be at

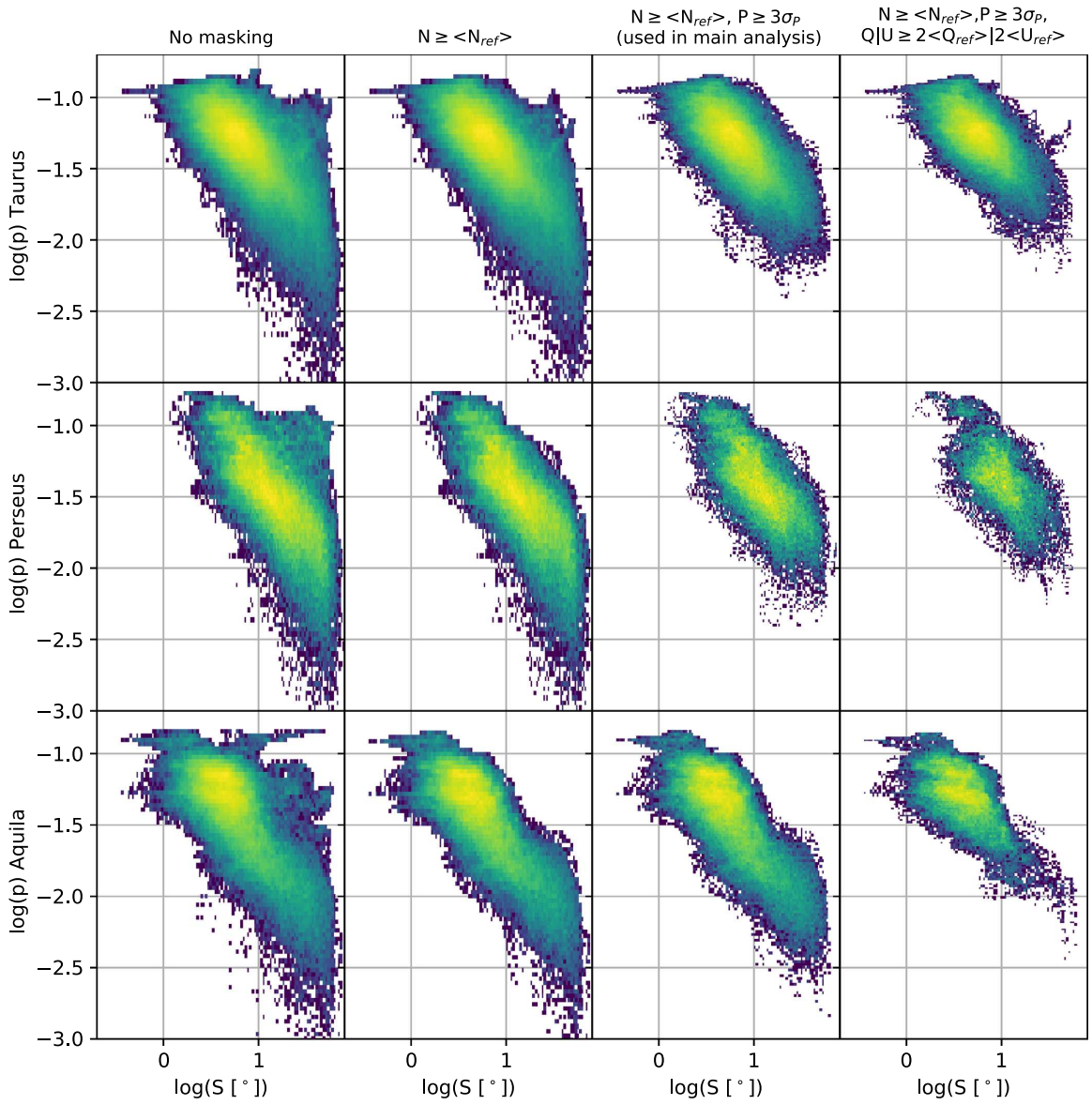

Figure A1. 2D histograms of the polarization fraction $log(p)$ and distribution of polarization angles log (S) for three of our *Planck* polarization maps: Taurus (top row), Perseus (middle row), and Aquila Rift (bottom row). Each of the columns shows how the p and S distributions change for different choices of the masking criteria. The leftmost column shows the distribution when no sightlines are masked, and the next column shows the distribution when the only masking criteria is that the sightlines used in the analysis must have a column density $N_{\rm H}$ that is greater than the average column density in a diffuse ISM field at the same Galactic latitude. The third column requires that the polarized intensity be at least a 3σ detection in addition to the column density threshold (this is what is used for the analysis in the main text of the paper). The rightmost column also requires that for each sightline used in the analysis, either Q or U must be at least two times as large as the RMS value of Q and U from the reference diffuse ISM field at the same Galactic latitude, which is the selection criteria used in Planck Collaboration XXXV (2016).

least 2× as bright as the emission in the same reference diffuse ISM field used to set the column density threshold. More specifically, the additional criteria for each sightline is that either

$$|Q| \geq 2|Q_{\rm ref}|, \tag{A1}$$

or

$$|U| \geq 2U_{\rm ref}, \tag{A2}$$

where $Q_{\rm ref}$ and $U_{\rm ref}$ are the RMS Q and U values in the reference diffuse ISM field. However, for many clouds this cut eliminates most of the sightlines (see e.g. Aquila in Fig. A1). It also leads to the rejection of most low-p/high-$\mathcal{S}$ sightlines, which further biases the sample to lower $\mathcal{S}$ values and shallower log(p) versus $log(\mathcal{S})$ slope indices.

Similarly, the same masking criteria also affect the relative distribution of polarization fraction p and column density ($N_{\rm H}$), as shown in Fig. A2. Applying the column density threshold criteria removes mostly high p sightlines. Applying the requirement that $P \geq 3\sigma_P$, removes mostly low p sightlines, but tends to remove somewhat higher p-values at lower column densities (e.g. for Taurus and Perseus). Applying the Planck Collaboration XXXV (2016) requirements from equations (A1) and (A2) removes even more low-p sightlines and tends to make the log(p) versus log(S) slope significantly more shallow.

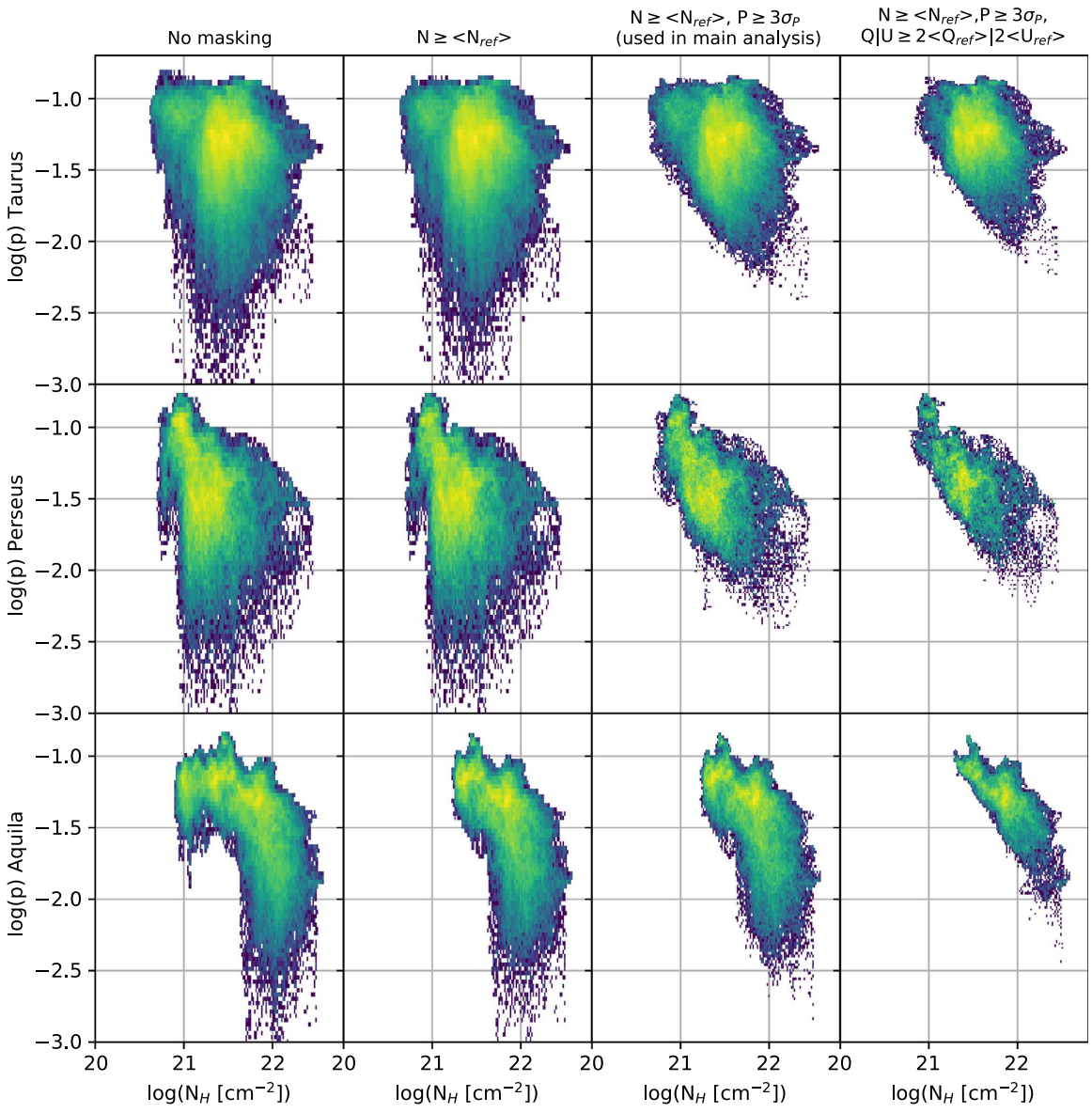

Figure A2. 2D histograms of the polarization fraction log(p) and log(N_H) for three of our *Planck* polarization maps: Taurus (top row), Perseus (middle row), and Aquila (bottom row). Each of the columns shows how the p and (N_H) distributions change for different choices of the masking criteria, as described in the caption for Fig. A1.

We can also check whether the sightline masking criteria affect the average polarization properties of the clouds. In Fig. A3, we show that the choice of sightline selection method certainly affects the median values of p, $\mathcal{S}$, and log ($N_{\rm H}$), but it does not typically change the relative trends between the clouds. The clouds that have the highest average polarization fraction with the sightline selection method used in the main paper text (Corona Australis and Chamaeleon-Musca), also have the highest polarization fraction if no sightline masking is applied, or if more aggressive polarization intensity masking is applied. Similarly, clouds that have high polarization angle dispersions, like Perseus, have high dispersion values for all of our tested sightline selection methods.

Finally, we discuss the effect of sightline selection on Fig. 8, where we compared the p versus $\mathcal{S}$ slope as a function of the geometric mean of $\mathcal{S}$, for the *Planck*-observed polarization maps, the BLASTPol polarization map of Vela C, and the synthetic models of the `Athena` MHD models presented in King et al. (2018). We argue that the mapping method used in the main text should give the best comparison data set for the simulations from King et al. (2018), as the synthetic observations only integrate over voxels from the post-shock region, which would be equivalent to the dense MC regions, and which has extremely high signal-to-noise polarization data.

Fig. A4 shows how the distribution of p-$\mathcal{S}$ slope versus mean $\mathcal{S}$ changes with sightline selection criteria. While the absolute values of the p-$\mathcal{S}$ slope do indeed change as more masking criteria are applied, the relative trends between the clouds are not significantly affected. Furthermore, all masking methods still show better agreement with the more turbulent Model A, rather than the highly sub-Alfvénic Model B. However, using the comparison shown in Figs 8 and A4 to constrain the inclination angle of the magnetic field will require a more careful accounting for the sightline selection effects when

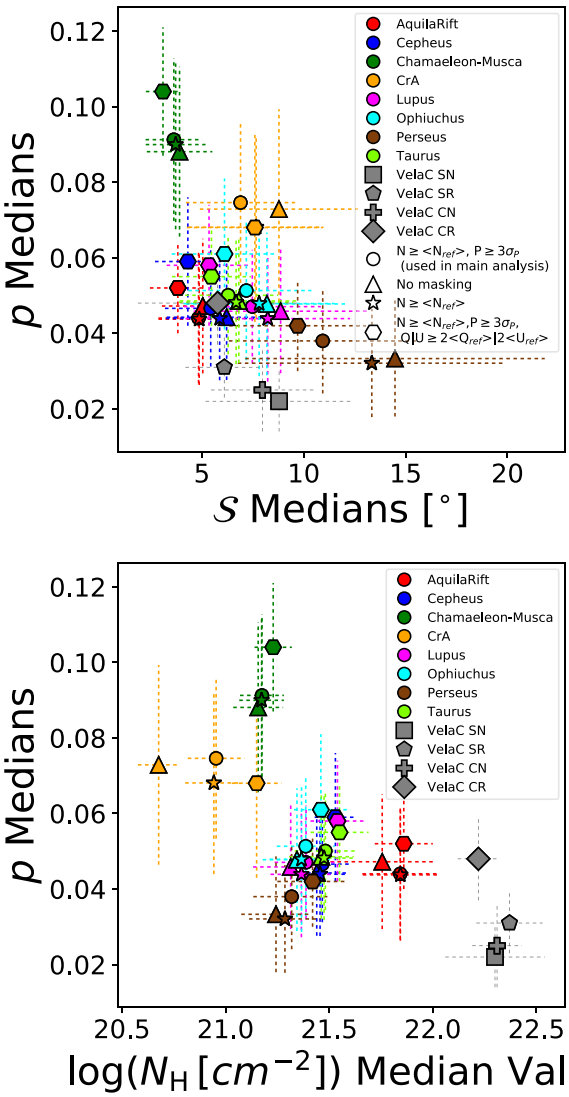

Figure A3. Comparison of the median polarization fraction p with polarization angle dispersion $\mathcal{S}$ (top panel) and the logarithm of hydrogen column density $\log(N_{\rm H})$ (bottom panel). This figure is similar to Fig. 7, except that for the *Planck* observed clouds we show the median values using the four different masking criteria discussed in Appendix A. The dotted lines indicate the median absolute deviations (MAD) for each quantity, and are intended to indicate the range of polarization values for each cloud.

comparing with synthetic observations, which is beyond the scope of this work.

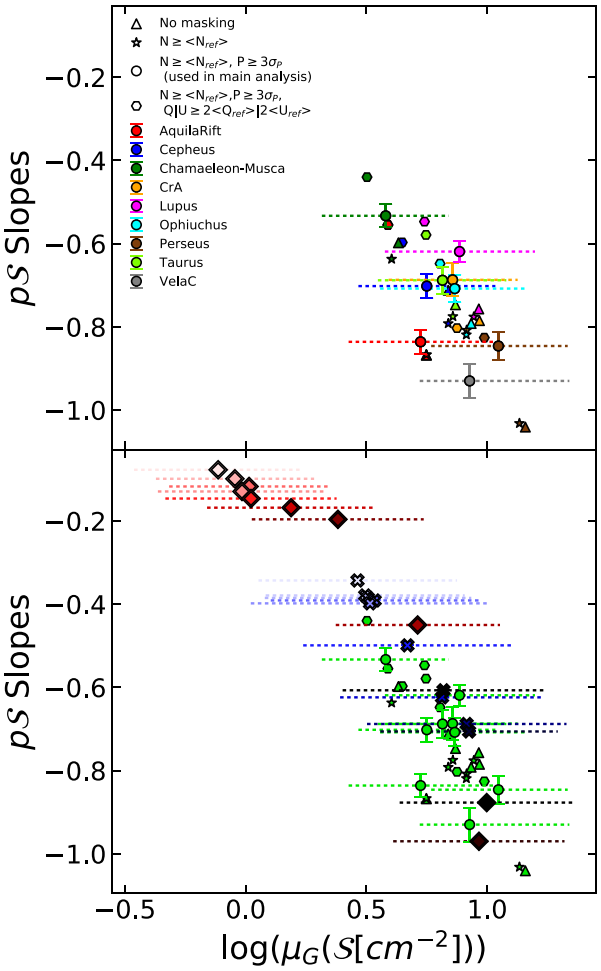

Figure A4. Plot of the fitted $\log(p)$ versus $\log(\mathcal{S})$ slope index compared to the logarithm of geometric mean polarization distribution $\mathcal{S}$, similar to Fig. 8, but comparing different masking strategies for the *Planck* data. In addition to the masking strategy used in the main paper text as described in Section 2.1 (the circles, $N_{\rm H}$ larger than the RMS $N_{\rm H}$ of a reference diffuse ISM field at the same Galactic latitude, and $P \geq 3\sigma_P$) we also show p-$\mathcal{S}$ slope versus $\mu_G(S)$ with no masking applied (the triangles), and column density threshold masking only (the stars). We also show p-$\mathcal{S}$ slope versus $\mu_G(\mathcal{S})$ using the same masking as is used in the main paper, but with the additional requirement that either Q or U be at least twice as large as the RMS Q or U of the diffuse ISM reference field as required by Planck Collaboration XXXV (2016) (hexagons). We show 16th and 84th percentiles of the $\mathcal{S}$ distribution (the dotted horizontal lines) only for the models and standard masking used in the main paper. The vertical error bars are the 3σ confidence intervals for the p-$\mathcal{S}$ slope fits derived from bootstrapping analysis described in Section 4.

This paper has been typeset from a TEX/LATEX file prepared by the author.

List of astronomical key words (Updated on 2020 January)

This list is common to *Monthly Notices of the Royal Astronomical Society, Astronomy and Astrophysics*, and *The Astrophysical Journal*. In order to ease the search, the key words are subdivided into broad categories. No more than *six* subcategories altogether should be listed for a paper.

The subcategories in boldface containing the word 'individual' are intended for use with specific astronomical objects; these should never be used alone, but always in combination with the most common names for the astronomical objects in question. Note that each object counts as one subcategory within the allowed limit of six.

The parts of the key words in italics are for reference only and should be omitted when the keywords are entered on the manuscript.

General
editorials, notices
errata, addenda
extraterrestrial intelligence
history and philosophy of astronomy
miscellaneous
obituaries, biographies
publications, bibliography
sociology of astronomy
standards

Physical data and processes
acceleration of particles
accretion, accretion discs
asteroseismology
astrobiology
astrochemistry
astroparticle physics
atomic data
atomic processes
black hole physics
chaos
conduction
convection
dense matter
diffusion
dynamo
elementary particles
equation of state
gravitation
gravitational lensing: micro
gravitational lensing: strong
gravitational lensing: weak
gravitational waves
hydrodynamics
instabilities
line: formation
line: identification
line: profiles
magnetic fields
magnetic reconnection
(magnetohydrodynamics) MHD
masers
molecular data
molecular processes
neutrinos
nuclear reactions, nucleosynthesis, abundances
opacity
plasmas
polarization
radiation: dynamics
radiation mechanisms:general
radiation mechanisms: non-thermal
radiation mechanisms: thermal
radiative transfer
relativistic processes
scattering
shock waves
solid state: refractory
solid state: volatile
turbulence
waves

Astronomical instrumentation, methods and techniques
atmospheric effects
balloons
instrumentation: adaptive optics
instrumentation: detectors
instrumentation: high angular resolution
instrumentation: interferometers
instrumentation: miscellaneous
instrumentation: photometers
instrumentation: polarimeters
instrumentation: spectrographs
light pollution
methods: analytical
methods: data analysis
methods: laboratory: atomic
methods: laboratory: molecular
methods: laboratory: solid state
methods: miscellaneous
methods: numerical
methods: observational
methods: statistical
site testing
space vehicles
space vehicles: instruments
techniques: high angular resolution
techniques: image processing
techniques: imaging spectroscopy
techniques: interferometric
techniques: miscellaneous
techniques: photometric
techniques: polarimetric
techniques: radar astronomy
techniques: radial velocities
techniques: spectroscopic
telescopes

Astronomical data bases
astronomical data bases: miscellaneous
atlases
catalogues
surveys
virtual observatory tools

Software
software: data analysis
software: development
software: documentation
software: public release
software: simulations

Astrometry and celestial mechanics
astrometry
celestial mechanics
eclipses
ephemerides
occultations
parallaxes
proper motions
reference systems
time

The Sun
Sun: abundances
Sun: activity
Sun: atmosphere
Sun: chromosphere
Sun: corona
Sun: coronal mass ejections (CMEs)
Sun: evolution
Sun: faculae, plages
Sun: filaments, prominences
Sun: flares
Sun: fundamental parameters
Sun: general
Sun: granulation
Sun: helioseismology
Sun: heliosphere
Sun: infrared
Sun: interior
Sun: magnetic fields
Sun: oscillations
Sun: particle emission
Sun: photosphere
Sun: radio radiation
Sun: rotation
(Sun:) solar–terrestrial relations
(Sun:) solar wind
(Sun:) sunspots
Sun: transition region
Sun: UV radiation
Sun: X-rays, gamma-rays

Planetary systems
comets: general

comets: individual: . . .
Earth
interplanetary medium
Kuiper belt: general

Kuiper belt objects: individual: . . .
meteorites, meteors, meteoroids
minor planets, asteroids: general

minor planets, asteroids: individual: . . .
Moon
Oort Cloud
planets and satellites: atmospheres
planets and satellites: aurorae
planets and satellites: composition
planets and satellites: detection
planets and satellites: dynamical evolution and stability
planets and satellites: formation
planets and satellites: fundamental parameters
planets and satellites: gaseous planets
planets and satellites: general

planets and satellites: individual: . . .
planets and satellites: interiors
planets and satellites: magnetic fields
planets and satellites: oceans
planets and satellites: physical evolution
planets and satellites: rings
planets and satellites: surfaces
planets and satellites: tectonics
planets and satellites: terrestrial planets
planet–disc interactions
planet–star interactions
protoplanetary discs
zodiacal dust

Stars
stars: abundances
stars: activity
stars: AGB and post-AGB
stars: atmospheres
(stars:) binaries *(including multiple)*: close
(stars:) binaries: eclipsing
(stars:) binaries: general
(stars:) binaries: spectroscopic
(stars:) binaries: symbiotic
(stars:) binaries: visual
stars: black holes
(stars:) blue stragglers
(stars:) brown dwarfs
stars: carbon
stars: chemically peculiar
stars: chromospheres
(stars:) circumstellar matter
stars: coronae
stars: distances
stars: dwarf novae
stars: early-type
stars: emission-line, Be
stars: evolution
stars: flare
stars: formation
stars: fundamental parameters
(stars:) gamma-ray burst: general
(stars:) **gamma-ray burst: individual: . . .**
stars: general
(stars:) Hertzsprung–Russell and colour–magnitude diagrams
stars: horizontal branch
stars: imaging
stars: individual: . . .
stars: interiors

stars: jets
stars: kinematics and dynamics
stars: late-type
stars: low-mass
stars: luminosity function, mass function
stars: magnetars
stars: magnetic field
stars: massive
stars: mass-loss
stars: neutron
(stars:) novae, cataclysmic variables
stars: oscillations *(including pulsations)*
stars: peculiar *(except chemically peculiar)*
(stars:) planetary systems
stars: Population II
stars: Population III
stars: pre-main-sequence
stars: protostars
(stars:) pulsars: general
(stars:) **pulsars: individual: . . .**
stars: rotation
stars: solar-type
(stars:) starspots
stars: statistics
(stars:) subdwarfs
(stars:) supergiants
(stars:) supernovae: general
(stars:) **supernovae: individual: . . .**
stars: variables: Cepheids
stars: variables: Scuti
stars: variables: general
stars: variables: RR Lyrae
stars: variables: S Doradus
stars: variables: T Tauri, Herbig Ae/Be
(stars:) white dwarfs
stars: winds, outflows
stars: Wolf–Rayet

Interstellar medium (ISM), nebulae
ISM: abundances
ISM: atoms
ISM: bubbles
ISM: clouds
(ISM:) cosmic rays
(ISM:) dust, extinction
ISM: evolution
ISM: general
(ISM:) HII regions
(ISM:) Herbig–Haro objects

ISM: individual objects: . . .
(except planetary nebulae)
ISM: jets and outflows
ISM: kinematics and dynamics
ISM: lines and bands
ISM: magnetic fields
ISM: molecules
(ISM:) photodissociation region (PDR)
(ISM:) planetary nebulae: general
(ISM:) **planetary nebulae: individual: . . .**
ISM: structure
ISM: supernova remnants

The Galaxy
Galaxy: abundances
Galaxy: bulge
Galaxy: centre
Galaxy: disc
Galaxy: evolution
Galaxy: formation
Galaxy: fundamental parameters
Galaxy: general
(Galaxy:) globular clusters: general
(Galaxy:) **globular clusters: individual: . . .**
Galaxy: halo
Galaxy: kinematics and dynamics
(Galaxy:) local interstellar matter
Galaxy: nucleus
(Galaxy:) open clusters and associations: general
(Galaxy:) **open clusters and associations: individual: . . .**
(Galaxy:) solar neighbourhood
Galaxy: stellar content
Galaxy: structure

Galaxies
galaxies: abundances
galaxies: active
galaxies: bar
(galaxies:) BL Lacertae objects: general
(galaxies:) **BL Lacertae objects: individual: . . .**
galaxies: bulges
galaxies: clusters: general

galaxies: clusters: individual: . . .
galaxies: clusters: intracluster medium
galaxies: disc
galaxies: distances and redshifts
galaxies: dwarf
galaxies: elliptical and lenticular, cD
galaxies: evolution
galaxies: formation
galaxies: fundamental parameters
galaxies: general
galaxies: groups: general

galaxies: groups: individual: . . .
galaxies: haloes
galaxies: high-redshift

galaxies: individual: . . .
galaxies: interactions
(galaxies:) intergalactic medium
galaxies: irregular
galaxies: ISM
galaxies: jets
galaxies: kinematics and dynamics
(galaxies:) Local Group
galaxies: luminosity function, mass function
(galaxies:) Magellanic Clouds
galaxies: magnetic fields
galaxies: nuclei
galaxies: peculiar
galaxies: photometry
(galaxies:) quasars: absorption lines
(galaxies:) quasars: emission lines
(galaxies:) quasars: general

(galaxies:) **quasars: individual: . . .**
(galaxies:) quasars: supermassive black holes
galaxies: Seyfert
galaxies: spiral
galaxies: starburst
galaxies: star clusters: general

galaxies: star clusters: individual: . . .
galaxies: star formation
galaxies: statistics
galaxies: stellar content
galaxies: structure

Cosmology
(cosmology:) cosmic background radiation
(cosmology:) cosmological parameters
(cosmology:) dark ages, reionization, first stars
(cosmology:) dark energy
(cosmology:) dark matter
(cosmology:) diffuse radiation
(cosmology:) distance scale
(cosmology:) early Universe
(cosmology:) inflation
(cosmology:) large-scale structure of Universe
cosmology: miscellaneous
cosmology: observations
(cosmology:) primordial nucleosynthesis
cosmology: theory

Resolved and unresolved sources as a function of wavelength
gamma-rays: diffuse background
gamma-rays: galaxies
gamma-rays: galaxies: clusters
gamma-rays: general
gamma-rays: ISM
gamma-rays: stars
infrared: diffuse background
infrared: galaxies
infrared: general
infrared: ISM
infrared: planetary systems
infrared: stars
radio continuum: galaxies
radio continuum: general
radio continuum: ISM
radio continuum: planetary systems
radio continuum: stars
radio continuum: transients
radio lines: galaxies
radio lines: general
radio lines: ISM
radio lines: planetary systems
radio lines: stars
submillimetre: diffuse background
submillimetre: galaxies
submillimetre: general
submillimetre: ISM
submillimetre: planetary systems
submillimetre: stars
ultraviolet: galaxies
ultraviolet: general
ultraviolet: ISM
ultraviolet: planetary systems
ultraviolet: stars
X-rays: binaries
X-rays: bursts
X-rays: diffuse background
X-rays: galaxies
X-rays: galaxies: clusters
X-rays: general
X-rays: individual: . . .
X-rays: ISM
X-rays: stars

Transients
(transients:) black hole mergers
(transients:) black hole - neutron star mergers
(transients:) fast radio bursts
(transients:) gamma-ray bursts
(transients:) neutron star mergers
transients: novae
transients: supernovae
transients: tidal disruption events